CONSTRAINING COSMOLOGICAL PARAMETERS AND TESTING THE ISOTROPY OF THE HUBBLE EXPANSION USING SUPERNOVAE Ia

Bachelor of Science Thesis

By

Konstantinos Nikolaos Migkas [1]

Thesis Supervisor:

Prof. Manolis Plionis

[1]*Physics Department, Aristotle University of Thessaloniki, Thessaloniki*

Greece 54124

February, 2015

This page intentionally left blank.

Abstract

In this thesis we use the latest *Union2.1* Supernovae Ia sample in order to put constraints to the basic cosmological parameters, such as the Dark Energy equation of state parameter w, the matter density Ω_m and the deceleration parameter q_0. We further use the angular coordinates of the SNe Ia in order to divide the sample in various independent groups, such as different solid angles, and test the isotropy of the Hubble expansion. Our main results are:

1. We have reproduced all the published results regarding the cosmological constrains put by the SNe Ia Hubble expansion probe.

2. We have estimated the deceleration parameter q_0 using the low-z SNe Ia ($z \leq 0.24$) and found $q_0 \simeq -0.501$ corresponding, for a flat Universe, to a matter density $\Omega_m \simeq 0.333$.

3. We have found that the Ω_m-w contours, provided by the SNe Ia analysis of different redshift ranges, cover distinct regions of the Ω_m-w solution space. We have also found, interestingly, that excluding the intermediate redshift range ($0.314 < z \leq 0.57$) does not affect significantly the cosmological constraints in the Ω_m-w plane, a fact that can have important implications for future observation strategies.

4. We have identified one sky region, with galactic coordinates $35^o < l < 83^o$ & $-79^o < b < -37^o$, containing 82 SNe Ia (15% of total with $z \geq 0.02$), that shares a different Hubble expansion behaviour indicating a possible anisotropy, if confirmed. We have excluded as a possible cause systematic effects related to the different surveys that constitute the *Union2.1* set. An alternative explanation, that we will investigate in the future is the existence of a bulk flow that could affect significantly the redshifts of the specific SNe Ia.

Περίληψη

Σε αυτή την εργασία χρησιμοποιούμε το πιο πρόσφατο σετ Υπερκαινοφανών Τύπου Ια *Union2.1* προκειμένου να υπολογίσουμε τα όρια τιμών των βασικών κοσμολογικών παραμέτρων, όπως ο βαροτροπικός δείκτης w της Σκοτεινής Ενέργειας, η πυκνότητα ύλης Ω_m και ο παράγοντας επιβράδυνσης q_0. Επίσης, χρησιμοποιούμε τις γαλαξιακές συντεταγμένες των Υπερκαινοφανών Ια για να χωρίσουμε το δείγμα σε διάφορες ανεξάρτητες ομάδες, όπως π.χ. σε στερεές γωνίες, και να ελέγξουμε την ισοτροπία της διαστολής Hubble. Τα βασικά μας αποτελέσματα είναι:

1. Αναπαράγαμε όλα τα δημοσιευμένα αποτελέσματα που αφορούν τα όρια των κοσμολογικών παραμέτρων που προκύπτουν από τους Υπερκαινοφανείς Ια.

2. Υπολογίσαμε τον συντελεστή επιβράσυνσης q_0 χρησιμοποιώντας τους Υπερκαινοφανείς Ια με χαμηλές ερυθρομεταθέσεις ($z \leq 0.24$) και βρήκαμε $q_0 \simeq -0.501$, που αντιστοιχεί, για ένα επίπεδης γεωμετρίας Σύμπαν, σε μια πυκνότητα ύλης $\Omega_m \simeq 0.333$.

3. Βρήκαμε ότι οι ισοπίθανες επιφάνειες των Ω_m-w που προκύπτουν από την ανάλυση των Υπερκαινοφανών Ια για διαφορετικά όρια ερυθρομεταθέσεων, καλύπτουν ανόμοιες περιοχές στην περιοχή λύσεων των Ω_m-w. Επίσης, με πολύ ενδιαφέρον, βρήκαμε ότι αν αποκλείσουμε τις μεσαίες ερυθρομεταθέσεις ($0.314 < z \leq 0.57$, 1/4 του συνολικού δείγματος) δεν επηρεάζονται σημαντικά τα αποτελέσματα και τα όρια των κοσμολογικών παραμέτρων.

4. Ανιχνεύσαμε μία περιοχή του ουρανού με γαλαξιακές συντεταγμένες $35^o < l < 83^o$ · $-79^o < b < -37^o$ στην οποία περιέχονται 82 Υπερκαινοφανείς Ια (το 15% του συνολικού δείγματος με $z \geq 0.02$) η οποία χαρακτηρίζεται από μια διαφορετική διαφορά στην διαστολή υποδεικνύοντας μια πιθανή ανισοτροπία στη διαστολή, αν τελικά επιβεβαιωθεί. Αποκλε;ισαμε ως πιθαν;η αιτ;ια ;ενα συστηματικ;ο σφ;αλμα που σχετ;ιζεται με διαφορετικο;υς καταλ;ογους δεδομ;ενων τα οπο;ια απαρτ;ιζουν το δε;ιγμα *Union2.1*. Μια εναλλακτική εξήγηση που θα εξετάσουμε στο μέλλον, είναι η ύπαρξη μιας συνεκτικής ροής που θα επηρέαζε τις ερυθρομεταθέσεις των δεδομένων.

Acknowledgements

I would like to express my deep gratitude to Prof. Plionis Manolis for guiding and helping me throughout this thesis. He was always more than willing to spent time with me in order to solve my queries. His deep knowledge in the field of observational cosmology and his ideas for this project played a key role in completing it. I am also thankful to Maria Manolopoulou who provided me with her valuable help about programming tools at the beginning of my work. Finally, I owe a lot to my lovely girlfriend and fellow student Eftychia Madika for all her constructive advice, for her daily support and for believing so much in me.

Contents

1 Introduction

It is well-known that we live in the Golden Age of *Cosmology*. The amount of observational data available is higher than ever. The detailed observations of the cosmos in the 20th century has changed dramatically our ideas for it. Millions of galaxies were discovered, we realized that the Universe is expanding, we found that there are huge amount of Cold Dark Matter not seen whose nature we still do not know and we predicted and confirmed the existence of Cosmic Microwave Background (CMB) radiation. However, maybe the biggest breakthrough of all, was the discovery by Saul Perlmutter, Adam Riess and Brian P. Schmidt in 1998 that the expansion of the Universe is accelerating, something completely contrary to what was believed until then. Ever since, the cosmology community has devoted a large amount of research in order to understand the cause for the accelerated expansion as well as the nature of the Dark Matter.

1.1 Basics of Dynamical Cosmology

One of the main tools we use to study the dynamical behaviour of the Universe are the *Friedmann equations*. Alexander Friedmann in 1922, achieved, using Einstein's field equations of gravity to derive a set of equations that described the dynamical behaviour of the Universe. The content of the Universe is assumed to be a homogeneous perfect fluid, that is a very good approximation to reality, according to the Cosmological Principle and the Robertson-Walker metric, which assumes homogeneity and isotropy. Therefore, these equations describe homogeneous and isotropic FLRW[1] models and they are:

$$H^2 = \frac{8\pi G \rho}{3} - \frac{kc^2}{\alpha^2} + \frac{\Lambda c^2}{3}$$

$$\dot{H} + H^2 = -\frac{4\pi G}{3}\left(\rho + \frac{3P}{c^2}\right) + \frac{\Lambda c^2}{3}$$

(1.1)

where $H \equiv \dfrac{\dot{\alpha}}{\alpha}$ is the Hubble parameter, with α being the scale factor of the Universe, G

---

[1]Friedmann-Lemaítre-Robertson-Walker

the gravitational constant, c the speed of light, ρ the mass density of the total cosmic (matter and radiation) fluid, Λ the cosmological constant and $k = 0, \pm 1$ is depended of the spatial curvature of the Universe. We have $k = 0$ for a spatially flat Universe and $k = +1, -1$ for a positively or negatively curved Universe respectively. Using eq. (1.1) we can have:

$$1 = \frac{8\pi G\rho}{3H^2} - \frac{kc^2}{\alpha^2 H^2} + \frac{\Lambda c^2}{3H^2}$$

$$= \frac{8\pi G}{3H^2}[\rho + \rho_k + \rho_\Lambda] \Rightarrow \tag{1.2}$$

$$1 = \Omega_m + \Omega_k + \Omega_\Lambda$$

where Ω_m, Ω_k, Ω_Λ are the fractional densities of matter, curvature and the cosmological constant or *Dark Energy*. Dark Energy (hereafter DE) is the term we use for this hypothetical fluid (with a negative equation of state parameter) that is expressed by Ω_Λ and seems to dominate the Universe in terms of mass-energy density. From eq. (1.1) we can find the total density (of all source terms mass, radiation, cosmological constant and curvature), and this is

$$\rho_{tot} = \frac{3H^2}{8\pi G} \approx 10^{-29} \ gr/cm^3$$

for this era. Thus, each density parameter is $\Omega_i = \dfrac{\rho_i}{\rho_{tot}}$. Combining the two parts of eq. (1.1) we can derive the continuity equation, that describes the changes of mass-energy density over time:

$$\dot{\rho} + 3\frac{\dot{\alpha}}{\alpha}\left(\rho + \frac{P}{c^2}\right) = 0 \Rightarrow$$

$$\dot{\rho} = -3H\left(\rho + \frac{P}{c^2}\right) \Rightarrow \tag{1.3}$$

$$\dot{\rho} = -3H\rho(1 + w)$$

where $P = wc^2\rho$, the equation of state of a perfect fluid and w the equation of state

parameter. Finally, we can define the *deceleration parameter*

$$q = -\frac{\ddot{\alpha}\alpha}{\dot{\alpha}^2} = -\left(1 + \frac{\dot{H}}{H^2}\right) \tag{1.4}$$

Since 1998, thanks to the work of S. Perlmutter, A. Riess and B. P. Schmidt we know that $q_0 < 0$, which means that the expansion of the Universe is accelerating, and not decelerating as would happen if our Universe contained only matter, baryonic or not. For this to happen, it must be $\dot{H} > 0$ or in other words $\Lambda > 0$. Generally, the second derivative of the cosmological scale factor must be $\ddot{\alpha} > 0$. We have to assume that there is some form of a perfect fluid, DE, with $w < -1/3$ in order to have an accelerating expansion. For baryonic and non-baryonic matter we have $w = 0$ and for the curvature, $w = -1/3$.

From the Friedmann and continuity equations, we can easily derive an equation that describes how the value of the Hubble parameter depends on the density parameters, the DE equation of state parameter and redshift z (or time):

$$H(z) = H_0\sqrt{\Omega_m(1+z)^3 + \Omega_k(1+z)^2 + \Omega_\Lambda \exp\left(3\int_0^z \frac{1+w(x)}{1+x}\,\mathrm{d}x\right)} \tag{1.5}$$

where $H_0 = 70 \; km/s/Mpc$ is the value of the Hubble parameter at this time. The prevailing values of all these parameters according to the latest data are $\Omega_m \approx 0.3$, $\Omega_k \approx 0$, $\Omega_\Lambda \approx 0.7$ and $w \approx -1$.

For example, for these exact values, when $z = 1$ (or 7.7×10^9 years ago) it was $H(z=1) = 123.2 \; km/s/Mpc$ while for a matter-dominant Einstein-de Sitter Universe, it would be $H(z) = 198 \; km/s/Mpc$. Finally, as shown in eq. (1.1), (1.3) and (1.5), for a Λ-dominated Universe with $w = -1$, the Hubble parameter would be constant throughout time.

1.2 Taking advantage of standard candles

We characterize as *standard candles* some astrophysical objects which have a known constant luminosity which is independent of spatial position and time. This gives as
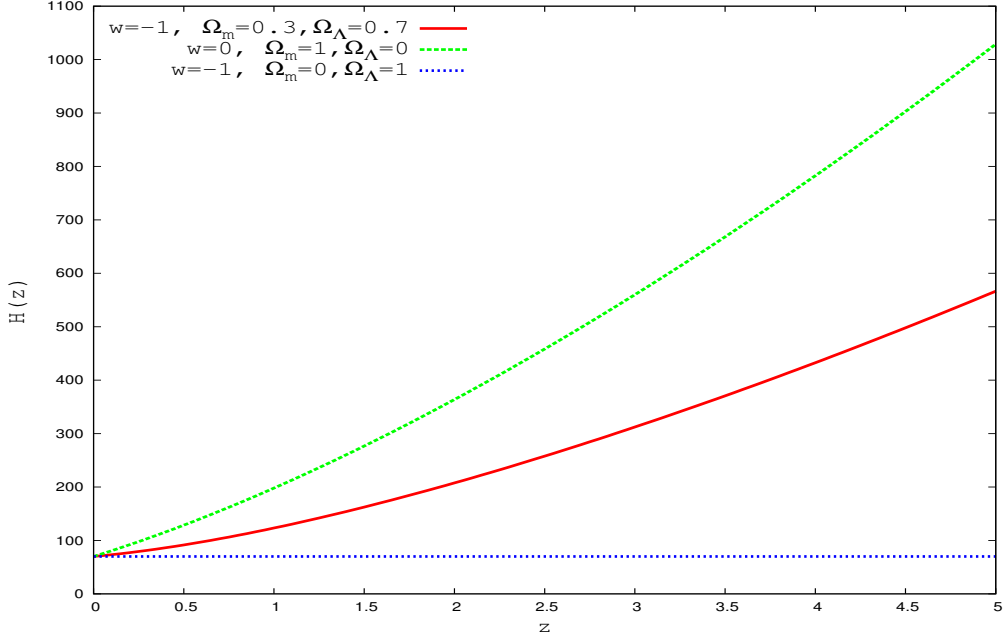
Figure 1: . The Hubble parameter as evolves with the redshift for Einstein-de Sitter model (green dashed line), ΛCDM model (red line) and de Sitter model (blue dashed line).

the huge advantage of knowing the absolute magnitude M of the object. The most common standard candles are the *Cepheid variables* and the *Supernovae of Type Ia* (SNe Ia). Cepheid variables are used to measure the distances of their host galaxies up to 30 Mpc and to calculate the Hubble constant H_0. On the other hand, SNe Ia are used for cosmological reasons and cosmological distances. If we measure the apparent magnitude m of a standard candle, then knowing its luminosity means that we know its *distance modulus* μ, defined as:

$$\mu = m - M = 5 \log d_L + 25 \tag{1.6}$$

where d_L is the luminosity distance of the object in Mpc. It is obvious that for standard candles, since we know M and we can easily measure m, we can calculate the observational distance modulus of the object μ_{obs} while we also measure the object's redshift z. On the other hand, we can theoretically calculate the luminosity distance d_L and of course the distance modulus μ_{th} for a given model. For a Universe with a non-flat geometry ($\Omega_k \neq 0$), d_L is defined as:

$$d_L = \frac{c(1+z)}{\sqrt{|\Omega_k|}} \sinh\left[\sqrt{|\Omega_k|} \int_0^z \frac{\mathrm{d}x}{H(x)}\right] \tag{1.7}$$

while for a flat Universe ($\Omega_k = 0$) is:

$$d_L = c(1+z) \int_0^z \frac{\mathrm{d}x}{H(x)} \tag{1.8}$$

Luminosity distance depends strongly on the cosmological model that we use, since the Hubble parameter within the integral contains all the cosmological parameters that we are interested in. Using various methods we can estimate the values of the cosmological parameters for which the theoretical expected μ_{th} gets as close as possible to the observational μ_{obs}. We analyse the method we use in this thesis, the reduced χ^2, in the Appendix.

1.3 How SNe Ia are produced?

The mechanism that leads to a supernova explosion of type Ia, is thought to be the same, independent of the time and location of the Universe that it occurs. SNe Ia appear in *binary star systems*. When one of the stars consumes all its fuel and thermonuclear fusing is not possible anymore, the star collapse under its own gravity since thermal pressure cannot support the outer layers. It passes from several stages of stellar evolution (i.e. red subgiant, giant etc.) that depend on the star's original mass. For stars that their mass, when they enter the main sequence is, $M \leq 5\ M_\odot$ their final state is that of an *white dwarf*. These are almost the 90% of all known stars.

White dwarfs are the product of the deterrence of the gravitational collapse of a star with ordinary mass by the pressure of *degenerate electrons* of its core (Varvoglis, Seiradakis 1994). The interior of the white dwarf mainly consists either of helium (He) for those with an original star mass of $M \leq 3\ M_\odot$, or of a mix of carbon and oxygen (C-O) for those with an original star mass of $3\ M_\odot < M \leq 5\ M_\odot$. The typical values of mass, density, radius and temperature of a white dwarf are $M \sim 0.7\ M_\odot$, $\rho \sim 10^6\ gr/cm^3$,

$R \sim 7000 \ km$ and $T \sim \ 10^6 - 10^7 K$ respectively. Since the gravitational pressure at the center of the white dwarf is approximately given by

$$P_c \approx \frac{3}{8\pi} \frac{GM^2}{R^4} \tag{1.9}$$

then for $M = 1 \ M_\odot$ and $R = 6000 \ km$ we obtain $P_c \approx 7.7 \times 10^{22} \ dyn/cm^2$. Matter in the interior of white dwarfs is fully ionized.

Due to the *Pauli exclusion principle* that states that two identical fermions cannot occupy the same quantum state at the same time and *Heisenberg's uncertainty principle*, that states $\Delta x \cdot \Delta p_x \geq h$, with Δx and Δp_x the uncertainties of the position and momentum of the free particles respectively and h is the Planck constant, the free electrons in the interior of the white dwarf have a non-zero kinetic pressure. This *degenerate electron pressure* is larger than the thermal pressure for more than an order of magnitude. Since the radius of a white dwarf is inversely proportional to its mass, for high-mass white dwarfs (more electrons, less space) the space that corresponds to each electron Δx decreases, so Δp and electrons velocity increase. Of course the velocity of the electrons cannot be larger than the speed of light, so it has an upper limit. For relativistic electrons (high-mass white dwarfs) the degenerate electron pressure is

$$P_e = \frac{1}{8} \left(\frac{3}{\pi} \right)^{1/3} hc \left(\frac{\rho}{\mu_e m_p} \right)^{4/3} \tag{1.10}$$

where m_p is the proton mass, $\mu_e = A/Z \approx 2$ is the mean molecular weight for a carbon-oxygen white dwarf, ρ the average density and c the speed of light. For the same values of mass and radius as before we obtain $\rho = 2.2 \times 10^{22} \ gr/cm^3$ and thus the degenerate electron pressure is $P_e \approx 10^{23} \ dyn/cm^2$. As we can see this quantum electron pressure is capable of resisting the gravitational collapse.

There is a limit of mass though that gravitational pressure becomes so powerful that degenerate electron pressure is unable to resist it. This mass limit is called *Chandrasekhar limit*. Its value can be found by equating the gravitational pressure with the quantum pressure. For $P_c = P_e$ we obtain a mass limit, independent of the radius R, which is

$M_{ch} \approx 1.44 \, M_\odot$. A white dwarf cannot have $M \geq M_{ch}$. Of course this value of M_{ch} applies for slow rotating white dwarfs. If someone considers a rapidly rotating white dwarf, then its mass can exceed this limit, M_{ch}. For a fast rotating C-O white dwarf M_{ch} is calculated to be 1.8 $M_\odot$.

Therefore, in a binary stars system, in which one of the stars becomes a C-O white dwarf, due to its high density (about 1 million times larger than the Sun's density), it has a tremendous gravity. At the surface of a typical white dwarf, we have $g_{WD} \approx 10^4 \, g_{Sun}$, where g_{Sun} is the surface gravity of Sun. Due to the white dwarf's strong gravitational field, it can gradually accrete mass from its companion star, which is usually thought to be a main sequence star, a red giant or a helium star (Yoon and Langer 2004), increasing its total mass. Since the rate of the accretion is usually $M \geq 10^{-7} \, M_\odot/yr$, this process can last for about 1 million years. As a result, the C-O white dwarf can finally reach the critical mass of M_{ch}. The corresponding central density is then $\rho \sim 10^9 \, gr/cm^3$. At this point, degenerate electron pressure can no longer resist the gravitational collapse. The white dwarf's radius decreases rapidly, causing the central pressure to increase and thermonuclear fusion of burning carbon and oxygen take place in its core. This energy-producing reactions are:

$$^{12}_{6}C + ^{12}_{6}C \rightarrow ^{20}_{10}Ne + ^{4}_{2}He + 4.6 \; MeV$$

$$^{16}_{8}O + ^{16}_{8}O \rightarrow ^{28}_{14}Si + ^{4}_{2}He + 9.6 \; MeV$$
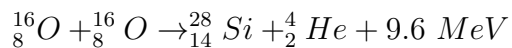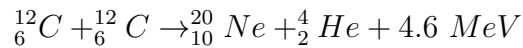
Carbon is the main source of energy since it burns completely, unlike oxygen. The total energy that is released by these reactions is $E \sim 10^{44} \, J$, and as a result the star explodes. This explosion is what we call a Type Ia Supernova (SN Ia). As expected, this large amount of energy leads to a rapid increase of the luminosity L and correspondingly to the absolute magnitude M. Since the production mechanism for SNe Ia is always the same, the peak luminosity of all SNe Ia is considered to be the same, not depending on time (redshift) and place (coordinates). This is the reason why they are considered *standard candles*. Their typical values are $L \approx 5 \cdot 10^9 \, L_\odot$ and $M \approx -19.3 \pm 0.03$ in the B-band. In many cases, a SN Ia may be even more luminous than its host galaxy.

1.4 The light curves of SNe Ia

The luminosity of each SN Ia evolves with time. The maximum luminosity appears a few dozen days after the explosion and then starts to drop until it fades completely in about a year. The light curves of many SNe Ia have deviations in terms of maximum absolute magnitudes. The faster the SN Ia luminosity drops with time, the lower the maximum luminosity. Thus, the SNe Ia with the most negative absolute magnitudes are fading with a lower rate than the others. This is usually called the time-scale "stretch-factor" (Kim, et al. 1997).
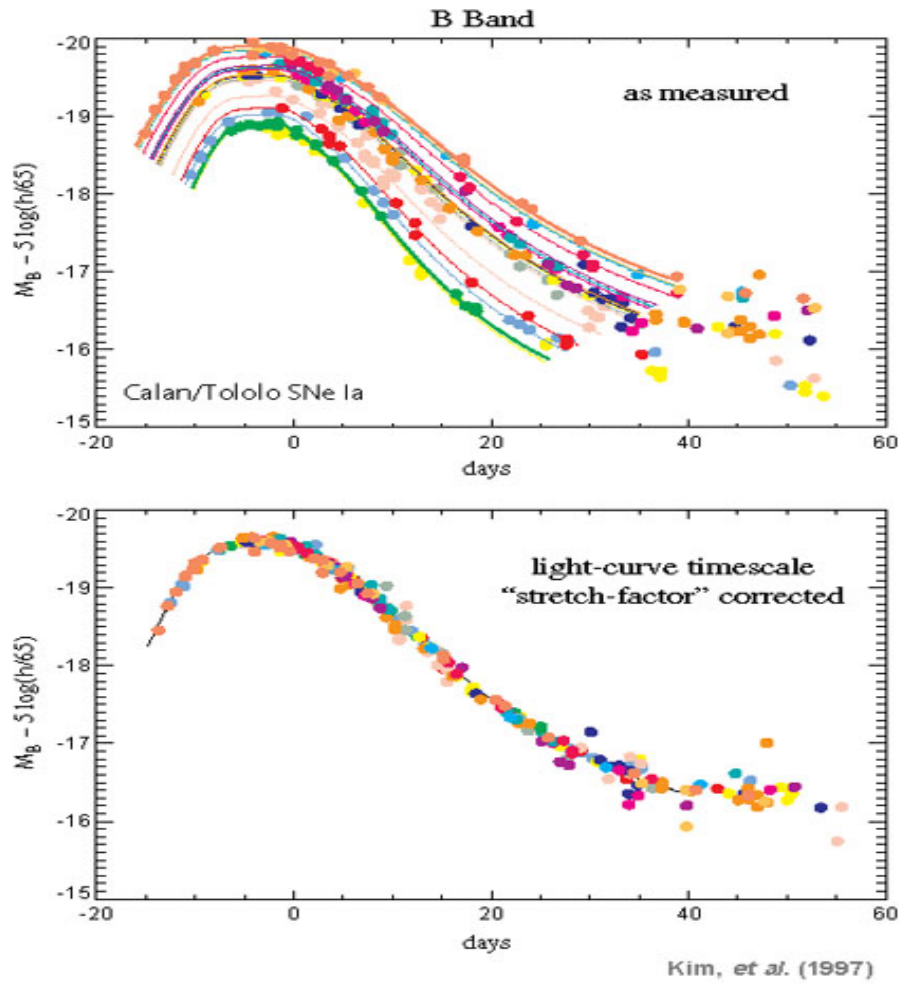

Figure 2: Absolute magnitude $M_B - 5\log{(h/65)}$ where $h = H_0/100$ in the B-band versus time from the peak luminosity. *Upper panel:* As measured. *Bottom panel:* After the correction for the timescale "stretch-factor".

15

In the upper panel of Figure 2 we can see the differences among various SNe Ia light curves. The vast majority of the light curves lie on the average light curve (the yellow one). After we stretch (or contract) the time scales of the other light curves and adjust the peak absolute magnitudes, we get the bottom panel of Figure 2, where all light curves coincide (Perlmutter et al. 1999).

In order to calculate exactly the correct absolute magnitude, someone have to know the distance of several SNe Ia by other methods, with great accuracy and measure their maximum apparent magnitudes. Then, from eq. (1.6) is easy to find the absolute magnitude M.

1.5   Cosmic and galactic dust

Interstellar dust is a very important component of the Universe, as it exists in abundance mostly in spiral galaxies (galactic dust), but there is also a lesser amount of gray dust in the intergalactic medium (cosmic dust). This dust interacts with the light emitted from the SNe Ia and causes a reddening of the light we receive since the extinction in the blue light is much larger. This extinction also causes the dimming of the SNe Ia and, if not corrected, it can lead to the luminosity distance to be overestimated compared with that of a Universe that contains no dust (Corasaniti 2006).

After the first indications for an accelerating expansion of the Universe in 1998, the extinction due to the cosmic gray dust was proposed as the reason for the observing dimness of the SNe Ia (Aguirre 1999a). This idea has been ruled out in the few next years for several reasons. First of all, for the Universe to be an Einstein-de Sitter Universe with $\Omega_m = 1$, $\Omega_\Lambda = 0$, it would need to have an intergalactic grey dust density of $\Omega_{IGD} \approx 5 \times 10^{-5}$ in order to explain the 0.5 mag deviation at $z = 0.7$ as being due to extinction. Such a density though, according to Riess et al. (1998), would cause redundant reddening and light dispersion in the SNe Ia and this is contrary to the observations. In addition, Perlmutter et al. (1999) found that the intrinsic dispersions at $z \approx 0.05$ (from Hamuy et al. 1996) and $z \approx 0.5$ (from Supernova Cosmology Project) were very similar (0.154 ± 0.04 and 0.157 ± 0.025 respectively) and this indicates that the processes that lead to

this dispersion are not affected by the redshift (Aguirre 1999b). Moreover, Perlmutter et al. (1998) studied the mean color difference between low-z and high-z data and found that they were identical, with $|E(B-V)|_{Hamuy} = 0.033 \pm 0.014$ and $|E(B-V)|_{SCP} = 0.035 \pm 0.022$, which shows that there is no significant correlation between the reddening and the redshift of the SNe Ia. As more SNe Ia discovered with time, the idea of intergalactic, cosmic dust being responsible for the deviation of the observations from a matter-dominated Universe was ruled out.

However, intergalactic dust does affect the incoming light of the SNe Ia to a certain degree. Cosmic dust can consists of grains of several materials and sizes, with lots of studies (Shustov & Vibe 1995; Davies et al. 1998; Bianchi & Ferrara 2005) suggesting that these sizes are between $0.02 \ \mu m - 0.2 \ \mu m$. Since the extinction due to dust is $A_B \sim 1/\alpha$, larger grains mean lesser extinction. Bianchi & Ferrara came to the conclusion that the distribution of the grains probably remains nearly flat (BF model) while the MRN model (Mathis, Rumpl, Nordsiek) describes the distribution of these grains as $N(\alpha) \propto \alpha^{-3.5}$. Corasaniti (2006) as well as Menard et al. (2009) and various other studies is find that the extinction caused by intergalactic dust is about $A_B \approx 0.01 \ mag$ at $z = 0.5$ for graphite and even smaller for silicate. At larger redshifts ($z \approx 1.5$) for the BF model we have $A_B \approx 0.08$ for graphite at and $A_B \approx 0.05$ for silicate, while for the MRN model extinction, it is about $0.02 \ mag$ larger for every material. In any case, the deviation in magnitude is within the uncertainties of the observations. If this extinction is not taken into account it leads the confidence regions of Dark Energy equation of state parameter w to more negative values (Corasaniti 2006) and the matter density Ω_m to lower values.

If we consider this phenomenon, then the real apparent magnitude m_{real} that we have to use in eq. 1.6 is $m_{real} = m_{obs} - A_B$. So, we calculate a smaller luminosity distance d_L and the values of the constrained cosmological parameters change. Ménard et al. (2010) use the Union sample of SNe Ia to put constraints in cosmological parameters with and without cosmic dust extinction in order to see how important is the influence of the dust in the extracted values of the cosmological parameters. They use high-$A_B(z)$ and low-$A_B(z)$ extinction models for ΛCDM and Quintessence DE models (hereafter QDE). For the QDE model, in both extinction cases they find a $\sim 2\%$ shift of Ω_m to higher values

and a $\sim 2.7\%$ shift of w to less negative values, compared to the parameters extracted in a dust-free Universe. All these changes are within 0.4σ confidence levels (see the section below about the statistical analysis method that we use). For the ΛCDM model they find a shift of $\delta\Omega_m = 0.02$ (7.2%) which corresponds to 0.55σ. Finally, Corasaniti (2006) adopts a cosmic dust model with graphite grains with size of $\alpha = 0.1\mu m$ in order to study the shift in the parameters using the Gold SNe Ia sample (Riess et al. 2004) and he finds a shift of $\delta w = 0.06$ (6.25%) that corresponds to 0.38σ.

Except for the intergalactic medium dust, there is another source of extinction, the interstellar medium dust inside the host galaxies of SNe Ia. The SNe Ia that are hosted by early-type galaxies have a more tight light curve distribution than those hosted by late-type galaxies (Riess et al. 1999; Sullivan et al. 2006) leading to a very useful uniformity. This occurs due to the older star populations of early-type galaxies which have a smaller range of masses than those in the late-type galaxies (Suzuki et al. 2012, hereafter S-12). However, the SNe Ia colors do not seem to be affected significantly by the type of their host galaxy.

As known, late-type galaxies contain notably more interstellar dust than early-type ones. This means that the SNe Ia that are observed in the late galaxies, have smaller statistical errors and several studies (Sullivan et al. 2003; 2010) have shown that these SNe Ia are slightly better standard candles than those hosted by late-type galaxies. After correcting for the color and light curve shape, the SNe Ia in early-type hosts seem to be about 0.14±0.07 mag brighter than those in later types (Hicken et al. 2009c; S-12). This factor can lead to important systematics errors if not corrected. Finally, SNe Ia in early-type hosts are more rare since, at lower-z it is observed that one in five SNe Ia occur in an early-type. (S-12).

1.6 Other cosmological probes

Except for SNe Ia, there are many other probes to study the cosmological parameters, like the temperature fluctuations of the CMB and Baryon Acoustic Oscillations.

- CMB radiation is the picture of our Universe when its age was about $350,000$ years old, when photon decoupling occured. It is *almost* isotropic, with small temperature fluctuations of $\Delta_T \approx 10^{-5}$ K that are considered to be one of the most powerful cosmological probes. The power spectrum of CMB temperature anisotropies versus their angular scale $\delta\theta$, or multipole moment l,
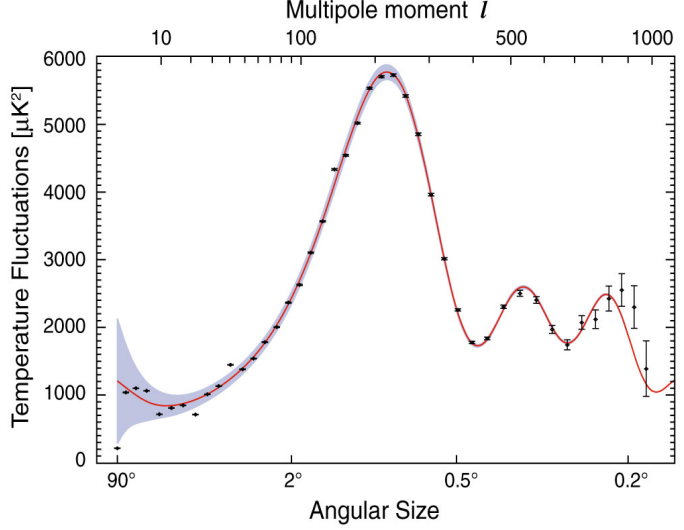

Figure 3: The CMB power spectrum as measured by *WMAP* until 2006

contains a wealth of cosmological information (Ryden, 2003) since its shape is determined by oscillations whose amplitudes and positions depend on the Universe's composition. For example, the position of the highest peak of the Δ_T versus $\delta\theta$ (or l) curve (at $l \approx 200^o$, $\delta\theta \approx 0.85^o$) determines the curvature of the Universe and is consistent with a spatially flat geometry, $k = 0$. The characteristic angular scale of the first peak in the CMB power spectrum is $\theta = \dfrac{r_s(z_{ls})}{d_A(z_{ls})}$ with $r_s(z_{ls})$ is the comoving size of the sound horizon at last scattering before the photon decoupling and $d_A(z_{ls})$ is the comoving angular distance to the last-scattering surface (Davis, Mörtsell, Sollerman et al. 2007). The anisotropies on larger angular scales derive from the influence of the gravitation of primordial density fluctuations in the Dark Matter distribution (Ryden, 2003). The ratio of heights between the first and second peaks shows us the amount of baryonic matter. Generally, using the peaks of the spectrum and using advanced computer simulations to provide the predictions of different models, we can put constraints in various parameters.

- The BAO provides a characteristic feature in the 2-p correlation function of galaxies, which results from the interplay between the radiation pressure and gravity in the photobaryonic plasma, coupled rigidly due to the Thomson scattering in the Universe before the recombination epoch (Basset, Hlozek, 2009). These two forces impose a system of standing sound waves within the photon-baryon fluid (Wu et al. 2015). At recombina-

tion the pressure on the baryons sharply declines because of the capturing of the free electrons by the atomic nuclei, and as a result the baryons have small over-densities at the sound horizon. The corresponding scale is the distance the sound wave had travelled in the plasma before the recombination (Wu et al. 2015). This distance can be measured from the CMB to be about 147 Mpc and it can be also measured from the clustering distribution of galaxies today. Therefore, the BAO scale is what we call a *standard ruler*. Standard rulers are cosmological probes with a well known size at a redshift z, or with a well known way of changing their sizes with redshift. So, by measuring the apparent diameter of the object, we can find the angular distance $d_A(z)$ for the given z as well as the luminosity distance $d_L(z)$, and using 1.7 we can constrain the cosmological parameters.

2 Theoretical expectations

In order to see how the distance modulus μ depends on the cosmological parameters and the redshift z, we first compare models with different w and Ω_m (we assume a flat universe, i.e. $\Omega_m + \Omega_\Lambda = 1$) with a reference ΛCDM model with $w = -1$ and $\Omega_m = 0.3$. Throughout this whole thesis we use $H_0 = 70 \ km/s/Mpc$. We also compare models with $\Omega_k \neq 0$ (non-flat Universe) with the same reference model and finally we use models with the Chevallier-Polarski-Linder (CPL) parametrization of the equation of state parameter.

We define the relative deviations of the distance modulus as

$$\Delta\mu = \mu_{model} - \mu_\Lambda \tag{2.1}$$

where μ is given by eq. (1.6).

2.1 Different QDE and ΛCDM models comparison

To begin with, we first compare cosmological models with different Ω_m with the reference model and then with different w. We firstly use spatially flat models ($\Omega_k = 0$). For the case of a constant w, the Hubble parameter, as we can see in eq. (1.5), is given by

$$H(z) = H_0\sqrt{\Omega_m(1+z)^3 + \Omega_k(1+z)^2 + \Omega_\Lambda(1+z)^{3(1+w)}} \tag{2.2}$$

We use four different values for each parameter:

As we can see in Figure 4, the relative deviations of the distance moduli in the left panel are much larger than those in the right panel. That indicates that it is easier to put limits to the values of Ω_m using SNe Ia with $z \geq 1$ if we assume a certain value of w, than limit the values of w for a certain Ω_m. This happens because changes in Ω_m affect the luminosity distance (and hence the distance modulus) more strongly than changes in w.
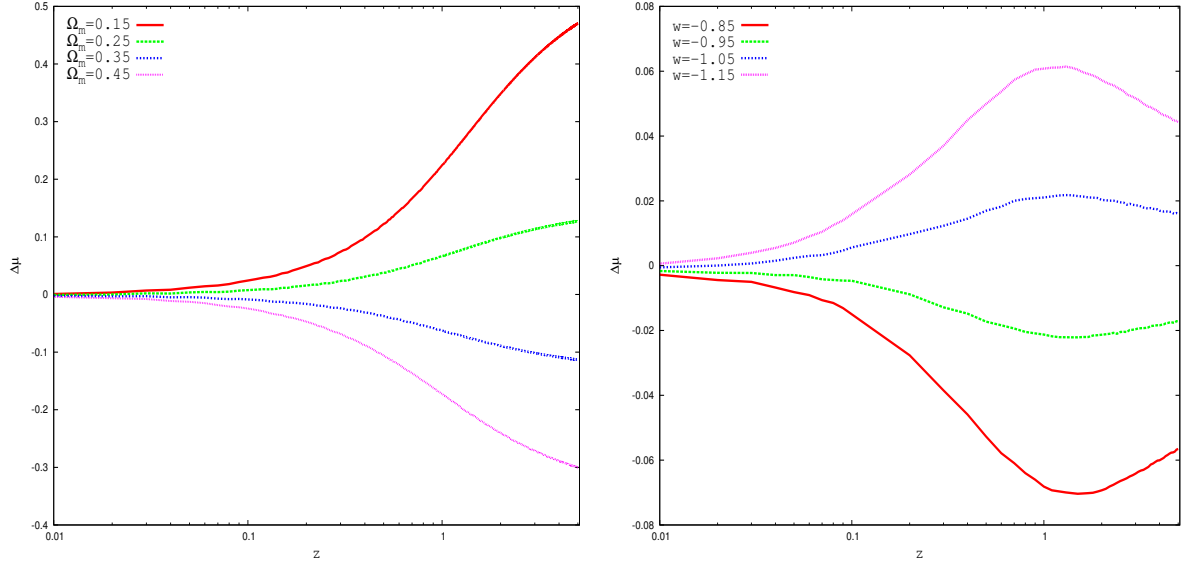
Figure 4: The expected distance modulus deviations $\Delta\mu$ vs. z *Left panel:* Between models with $w = -1$ and different $\Omega_m (= 0.15, 0.25, 0.35, 0.45)$ and the reference model ($w = -1$, $\Omega_m = 0.3$). *Right panel:* Between models with $\Omega_m = 0.3$ and different $w (= -0.85, -0.95, -1.05, -1.15)$ and the reference model ($w = -1$, $\Omega_m = 0.3$).

In addition, we can see that in the left panel there is no maximum relative deviation of the distance moduli. This happens because the first term under the square root containing Ω_m in eq. (2.2) is the most dominant of large redshifts. $\Delta\mu$ increases with a lower rate as z increases. The curvature of $\Delta\mu$ changes at $z \approx 0.9 - 1$.

In the right panel, the maximum deviation from the reference model occurs at $z \approx 1.3 - 1.4$. This happens for the same reason as above. The first term under the square root in $H(z)$ is getting stronger as z increases while the two models have the same Ω_m. As a result, for $z \geq 1.4$ any difference in $H(z)$ between the two models begin to eliminate.The curvature of $\Delta\mu$ changes at $z \approx 0.5$.

As can be derived from Friedmann equations and as shown here, lower values of Ω_m and w correspond to larger luminosity distances for the same z. This means that in a more "empty" Universe, or in a Universe with a more negative equation of state parameter, the radial velocity of any light source is lower for the same luminosity distance than in a Universe with a higher value of Ω_m or a less negative w.

2.2 Models comparison for a non-flat Universe ($\Omega_k \neq 0$)

In this subsection, we compare models with four different values for spatial curvature density ($\Omega_k = 1 - \Omega_m - \Omega_\Lambda$) with a reference *flat* ΛCDM model. We use the 95%-confidence limits for Ω_K as derived by the CMB measurements.

In the left panel of Figure 5, we see that for negatively curved models, the distance modulus μ is always larger than this of the reference model ($\Delta\mu > 0$). The values of Ω_K are the 95%-confidence limits as gives by Planck Collaboration (2014). For the positively curved models with $\Omega_k = 0.006$ and $\Omega_k = 0.008$ we have $\Delta\mu < 0$ until $z = 3.09$. For larger redshifts we have $\Delta\mu > 0$ while their lowest peaks are both at $z = 0.93$. It is noteworthy that for every model, negatively or positively curved, $\Delta\mu$ tends to rise. The relative magnitude deviations though are not large enough in order to exclude some values of Ω_k with our observations, except for the most negative one, $\Omega_k = -0.086$.

Specifically, for $\Omega_k > 0$, the maximum deviation is $\Delta\mu = -0.003$ for z=0.93 and $\Delta\mu = -0.0028$ for z=5. This strong degeneracy means that we cannot distinguish models with a very small $\Omega_k > 0$ from models with $\Omega_k = 0$. On the other hand, it is easier to test models with a significant $\Omega_k < 0$ using our observations due to the relatively high $\Delta\mu$. An interesting point is that the best fits given by all CMB surveys are provided for $\Omega_k < 0$.

2.3 Model comparison for CPL parametrization ($w = w(z)$)

Next, we use the CPL parametrization of equation of state parameter:

$$w(z) = w_0 + w_1 \frac{z}{1+z} \tag{2.3}$$

where w_0 and w_1 are constants. This form of $w(z)$ indicates that the relation between pressure P and density ρ, $\quad p = w(z)\rho$, of the Dark Energy, changes with time. In this case the Hubble parameter as defined in eq. (1.5) is given by

$$H(z) = H_0 \sqrt{\Omega_m(1+z)^3 + \Omega_k(1+z)^2 + \Omega_\Lambda(1+z)^{3(1+w_0+w_1)} \exp\left(-\frac{3w_1 z}{1+z}\right)} \qquad (2.4)$$
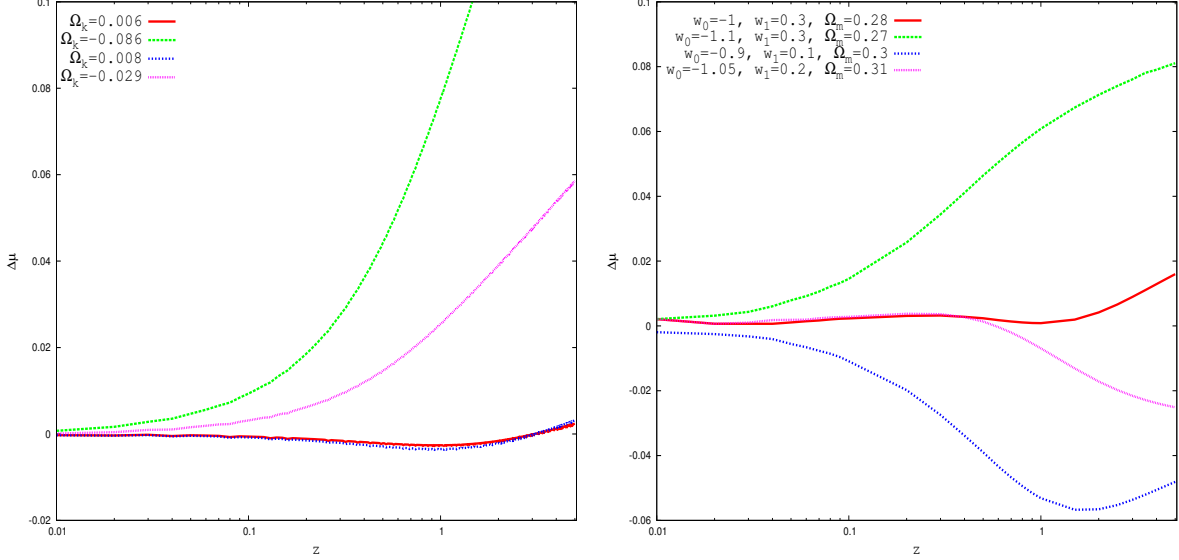

Figure 5: The expected distance modulus deviations $\Delta\mu$ vs. z. *Left panel:* Between models with ($w = -1$, $\Omega_m = 0.3$) and different Ω_k and the reference model ($\Omega_k = 0$). $\Omega_k(= -0.086, 0.006)$ are the 95%-confidence limits from *Planck+WMAP* CMB results while $\Omega_k(= -0.029, 0.008)$ are the 95%-confidence limits from *Planck+WMAP* CMB results and other cosmological probes. *Right panel:* Between spatially flat models with a combination of $w(z)$ and Ω_m and the reference ΛCDM model ($w = -1$, $\Omega_m = 0.3$)

In the right panel we have four models with a time varying equation of state parameter, $w(z)$. For a lower $w_0(= -0.9)$ value with respect to the reference model and a low positive $w_1(= 0.1)$ (blue-dotted line), it holds that $\Delta\mu < 0$ as expected. The lowest peak is again at $z \approx 1.3$, where Ω_m starts to play the biggest role in $H(z)$. On the other hand, for $w = -1.1$ and for a relatively large $w_1 = 0.3$ (green-dotted line), it holds that $\Delta\mu > 0$, but the lower value of $\Omega_m(= 0.27)$ has of course to do with this. Maybe the most important conclusion from the comparison , is the strong degeneracy that exists between the two other models (red and pink line). There is almost no difference until $z = 0.5$ and there is a very small difference of $\Delta\mu \approx 0.04\,mag$ up to $z = 5$. This is typical of how difficult it is to differentiate models with $w = w(z)$ instead of a constant w even if Ω_m is constrained with some other cosmological probe. Finally, as we have mentioned several times before,

24

the distance modulus deviations that is caused by different w are reduced as the redshift increases above some $z \sim 1.5$. That causes models with similar Ω_m's to have $\Delta\mu \approx 0$ at very high z's (which however is beyond any possibility of obtaining observable data).

3 The SNe Ia data

Union2.1 is the most recent compilation of SNe Ia of *Supernova Cosmology Project*(SCP). It is the largest one so far, as it first consisted of 833 SNe which were drawn from 19 different datasets. After the lightcurve quality cuts, 580 of them remained. All usability cuts are developed regardless of cosmological models.

3.1 Criteria of confirmation of SNe Ia type and quality cuts

Only one light curve filter was used for the fitting of *Union2.1's* data, the Spectral Adaptive Light curve Template (SALT2-1). SALT2-1 uses the whole set in order to calibrate empirical light curve parameters when, at the same time, it typically assumes a ΛCDM or QDE model. Unfortunately, a model assumption is necessary since it handles SNe Ia in distances which are larger than those required by the linear Hubble's law. However it has been verified that this does not bias the cosmological parameters fit.

As it stated at (S-12) these light curve parameters are

- a colour parameter c, which contains the intrinsic SN colour and reddening due to dust in its host galaxy (deviation of the mean $B - V$ color of the SN Ia)

- an overall normalization to the time dependent spectral energy distribution (SED) of a SN Ia, χ_0

- the deviation of the average light curve shape, χ_1 (or $s = \chi_1 + 1$)

The distance modulus is then:

$$\mu = m_B^{max} - M + \alpha\chi_1 - \beta c$$

with m_B^{max} the rest-frame peak magnitude in the B-band (P. Smale, 2010) and M the absolute magnitude in the same band with $c = \chi_1 = 0$. Also, SALT2 and SALT2-1 use $\alpha = 0.135$ and $\beta = 3.19$. The initial light curve standardization results in the best-fitting values for the time t_0 of maximum in the B-band light curves. SNe Ia with observation time t_{obs} significantly different (several days) from t_0 were excluded. In addition, SN Ia

candidates which have deviations from the best fit light curve model that are significantly larger than their uncertainties are rejected.

Some of the high-z SNe that were discovered by the Hubble Space Telescope (HST) Cluster Supernova Survey, were excluded because they do not have enough information in their light curves for their type to be determined unambiguously (S-12). SNe that are SNe Ia, are classified as secure, probable or plausible. A secure SN Ia has a spectrum that directly confirms that is a SN Ia. Any other SN has to satisfy two conditions: Firstly, its host galaxy should have spectroscopic, photometric and morphological properties consistent with those of an early-type galaxy with no detectable signs of recent star formation (S-12), and secondly its light curve shape should be more consistent with that of a SN Ia and inconsistent with any other known SN types. A probable SN Ia is one that does not have a secure spectrum but it satisfies one of the above two non-spectroscopic conditions that are required for a secure classification. Finally, a plausible SN Ia is one that has an indicative light curve but has not enough information to reject being of other types (S-12). The *Union2.1* further contains 12 secure SNe Ia and 2 probable ones with respect to the *Union2*, while there are two SNe Ia, one secure (SCP06U4) and one probable (SCP06K18) that are not included in the *Union2.1* sample.

3.2   Redshift distribution of the Union2.1 sample

In this analysis we only use SNe Ia with $z \geq 0.02$ in order to avoid uncertainties in their estimated distances due to the local bulk flow. Thus, we only use the 546 SNe Ia that have $z \geq 0.02$. *Union2.1* contains 23 SNe Ia more than the *Union2* sample, 21 of them with $z \geq 0.02$ and 10 of them with $z > 1$. These 10 SNe Ia were discovered by the Hubble Space Telescope (HST) Cluster Supernova Survey, as well as another 4 SNe Ia with $z \in [0.623, 0.973]$. Of these 14 SNe Ia, 6 are members of galaxy clusters and 8 are members of non-cluster galaxies. High-redshift SN Ia are extremely important in calculating the cosmological parameters, because at these redshifts, the differences of the various DE models are more significant, as we saw in the previous chapter.

From Figure 6 we see that the number of the observed SNe Ia decreases, as expected,
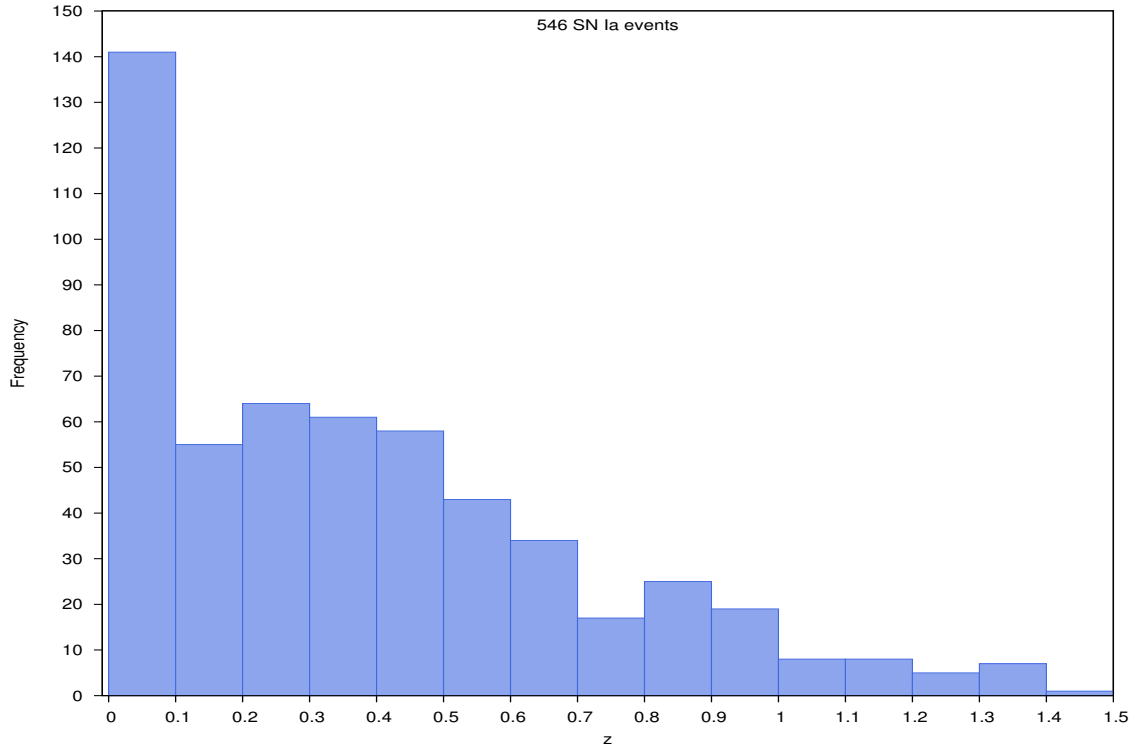
Figure 6: Redshift distribution of the 546 SNe Ia with $z \geq 0.02$ of the *Union2.1* sample.

with increasing z. Half of these 546 SNe Ia are for $z < 0.316$. There are 141 SNe Ia (25.82% of the sample we use) with $z \in [0.02, 0.1]$ while the 141 most distant ones have $z \in [0.562, 1.414]$. This distribution indicates the need for more high-redshift observations. Most of the data with $z < 0.4$ were taken from the Sloan Digital Sky Survey (SDSS) while most data with $z \in [0.4, 1]$ were taken by the SuperNova Legacy Survey (SNLS). For $z > 1$, data were taken from the HST survey.

3.3   Mapping the Union2.1 sample

The *Union2.1* catalogue contains the name of every SN Ia, its redshift z, the distance modulus μ, the corresponding 1σ statistical error, σ_{stat}, of μ and the probability of each SN Ia to be a member of a low mass galaxy. It does not contain the equatorial coordinates (right ascension α and declination δ) of SNe Ia, unlike *Union2*. However, in order to calculate the cosmological parameters for different sky regions, we needed the coordinates of the SNe Ia. Therefore, we took the equatorial coordinates from the *Union2* catalogue for the common SNe Ia with *Union2.1*, which are 556 (1 SN Ia is excluded from *Union2*)

and we found the coordinates of the rest SNe Ia from the following websites:

- `http://supernova.lbl.gov/2009ClusterSurvey/cands/`

- `http://www.cbat.eps.harvard.edu/lists/Supernovae.html`

- `http://astro.berkeley.edu/bait/public_html`

Knowing the equatorial coordinates of all the *Union2.1* SNe Ia, we can produce several *maps* of the sample which can help us to visualize its angular distribution. First we make the polar diagram of all data, with the redshift z being the radius and the right ascension α being the angle.
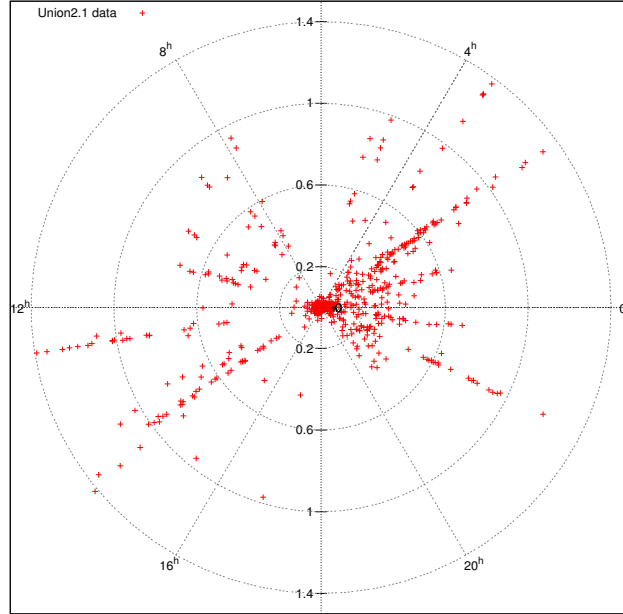

Figure 7: *Union2.1* data (580 SN Ia events) polar plot for redshift z and right ascension α

As we can see in Figure 7, the higher-z SNe Ia were detected preferentially along various directions, some of which contain more data than others. For example, there are 97 SNe Ia for $\alpha \in [2^h, 3^h]$, but there are only 26 SNe Ia for $\alpha \in [15^h, 20^h]$, 22 of them with $z < 0.15$.

A more useful representation of the sample's data is to produce the isosurface plot of the SNe Ia for α and δ (declination). Doing this, we will be able to see in which regions of the celestial sphere we have the most data.
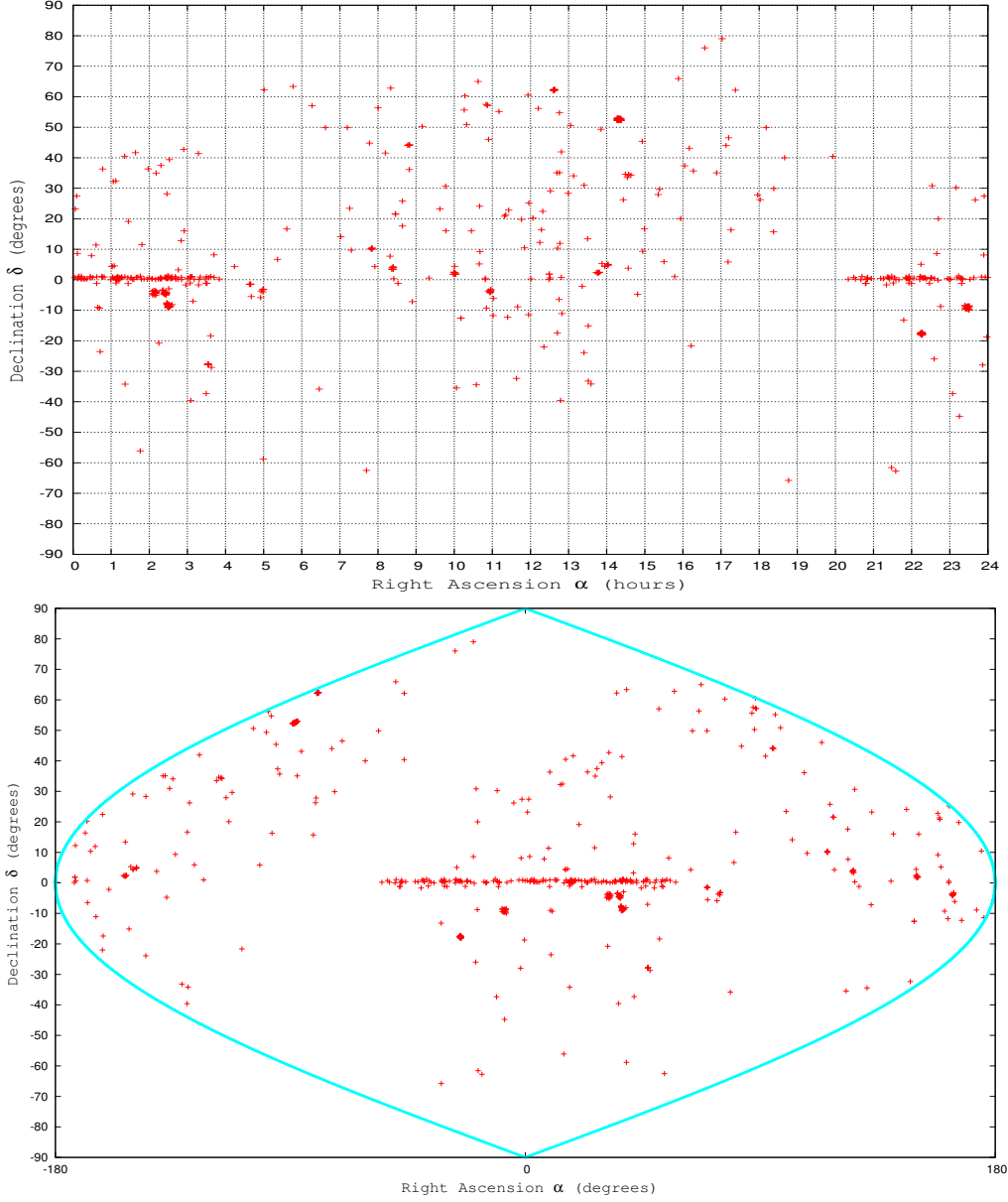
Figure 8: *Upper panel: Union2.1* data (580 SN Ia events) plot for equatorial coordinates α and δ. *Bottom panel:*The isosurface plot of the sample for α and δ

It is obvious from Figure 7 and Figure 8 that the data distribution is not uniform, since most SNe Ia have

$\delta \in [-10, 10]$. In addition, a lot of them have $\alpha \in [0^h, 4^h] \cup [20^h, 24^h]$[1].This happens because the observational campaigns cover very small solid angles of the sky (cluster of galaxies etc.), so they detect SNe Ia in tight regions instead of searching the whole sky, a fact which is dictated by the observational strategies necessary to detect SNe.

---

[1]From now on we are going to denote this region as $\alpha \in [20^h, 4^h]$

Specifically, there are 263 SNe Ia (45.3% of the sample) within the above δ limits. For a more narrow sky region with $\alpha \in [20^h, 4^h]$ and $\delta \in [-1.25^o, 1.25^o]$ (300 deg^2, 0.463% of the celestial sphere), the SDSS camera was used on the SDSS 2.5m telescope at the Apache Point Observatory (APO), in order to search for SNe Ia. The observations were made in the northern fall seasons of 2005 to 2007 (Betoule et al. 2014). That means that in these limits there are plenty of data with intermediate z's, as SDSS-II survey targeted SNe Ia with $z \in [0.05, 0.4]$.

We can produce the same plot for the galactic coordinates as well. In order to do that, we have to convert the equatorial coordinates α and δ into galactic longitude l and galactic latitude b. For this purpose we use the transformation equations:

$$l = 33^o + \arctan \left(\frac{\sin \delta \sin 62^o.6 + \cos \delta \sin (\alpha - 282^o.25) \cos 62^o.6}{\cos \delta \cos (\alpha - 282^o.25)} \right)$$

(3.1)

$$b = \arcsin \left[\sin \delta \cos 62^o.6 - \cos \delta \sin (\alpha - 282^o.25) \right]$$

where all coordinates are in degrees (if $\alpha = x^h$ then $\alpha = (15x)^o$).

In Figure 9 we can see that all the data with $\delta \in [-3, 3]$ from the previous graph, now form a characteristic "smile" in the southern galactic hemisphere. There are more data in the southern galactic hemisphere (351 SNe Ia) than in the northern (229 SNe Ia). As we mentioned above, we are going to use only the data with $z \geq 0.02$, to avoid the local bulk flow-based uncertainties. With this in mind, we are left with 335 SNe Ia south and 211 SNe Ia north. There are some "data-rich" areas in the south hemisphere, unlike the north hemisphere where the observations are more scattered and random.

There are no observations of SNe Ia for $b \in [-5, 5]$ due to the Milky way's plane. The large amount of dust and gas absorbs the emitted radiation in the optical band, not allowing us to observe possible SNe Ia.
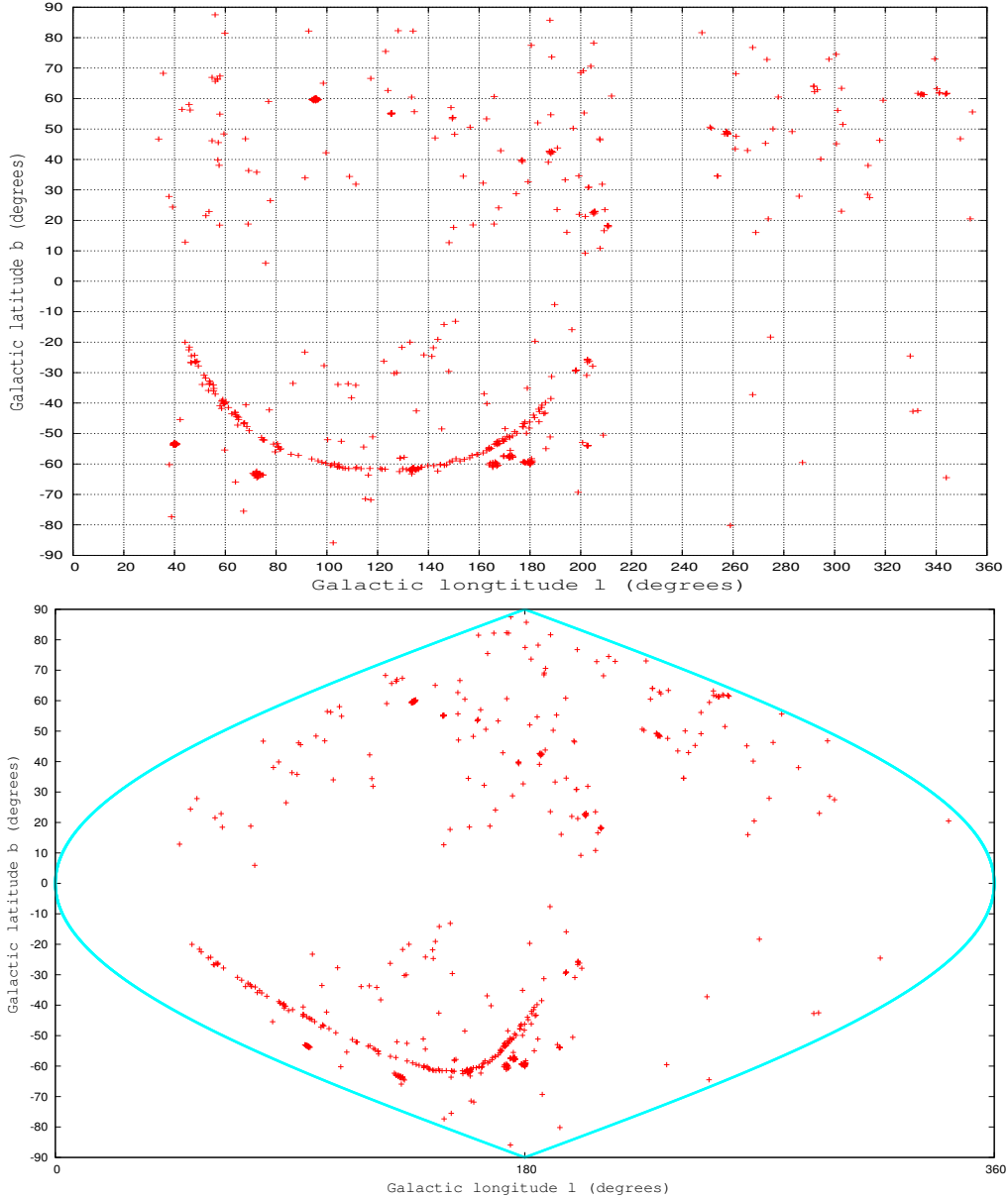
Figure 9: *Upper panel: Union2.1* data (580 SN Ia events) plot for galactic coordinates *l* and *b. Bottom panel:* The isosurface of the sample for *l* and *b*.

3.4 Statistical uncertainties of the distance moduli

In every analysis of data that are derived from an experiment or observation in any field of Physics, possible errors or uncertainties of the measurements can affect our conclusions. In order to have a full perspective of the statistical uncertainties of the distance moduli μ of the SNe Ia, we present their uncertainty distribution.

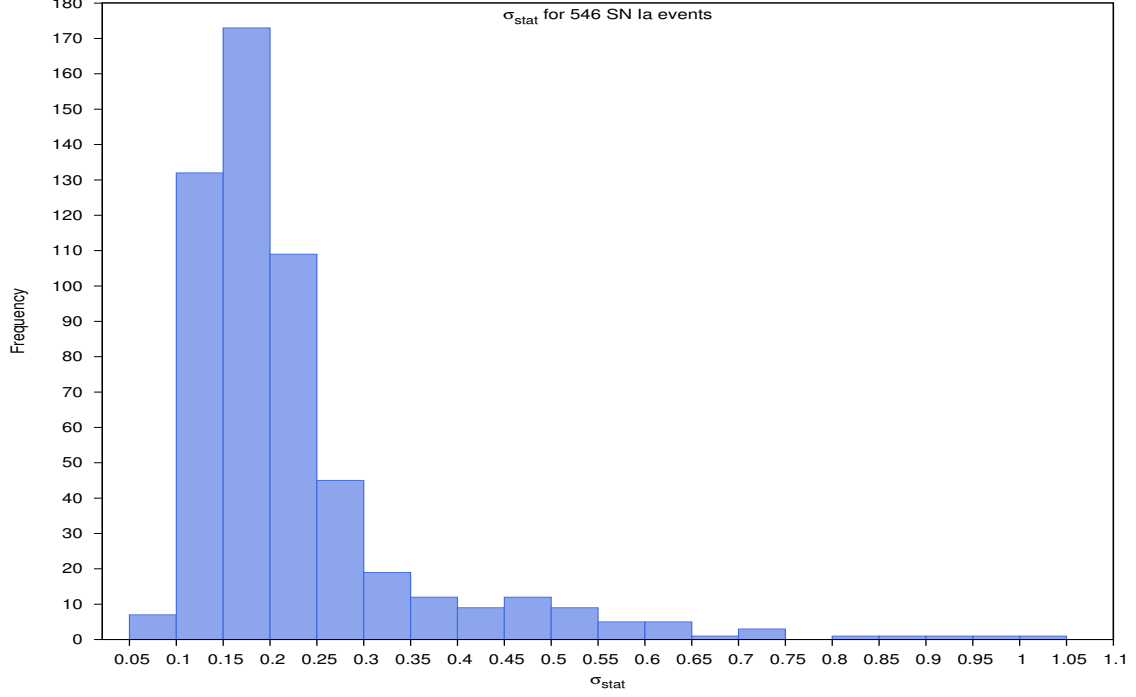In Figure 22, we see that the 1/3 of the data (173 SNe Ia) have a statistical uncertainty

Figure 10: Statistical uncertainty distribution of the 546 SNe Ia with $z \geq 0.02$ of the *Union2.1* sample.

of $\sigma_{stat} \in [0.15, 0.2]$ while 3/4 of the data (414 SNe Ia) have $\sigma_{stat} \in [0.1, 0.25]$. The mean value of it is $\overline{\sigma}_{stat} = 0.2229$. To compare these statistical errors with their corresponding distance moduli, we calculate the ratio $\frac{\sigma_{stat}}{\mu}\%$. There are only 46 SNe Ia with $\frac{\sigma_{stat}}{\mu} \geq 1\%$, and 4 of them have $\frac{\sigma_{stat}}{\mu} \geq 2\%$. On the contrary, there are 294 SNe Ia (53.8% of the sample) with $\frac{\sigma_{stat}}{\mu} \leq 0.5\%$, 7 of them with $\frac{\sigma_{stat}}{\mu} \leq 0.25\%$. Thus, we see that the distance modulus uncertainties for the *Union2.1* sample are minor for the most SNe Ia but there are exceptions for which the measurement of μ is not very trustworthy.

4   Cosmological parameters fitting

4.1   One-parameter models (Ω_m or w)

In order to fit our data with a model and extract the best values of the model parameters, we use the χ^2 minimization analysis. We change step-by-step our model parameters values within some limits and see which combination of them give

$\chi^2 = \chi^2_{min}$. Then, we estimate the uncertainty of these parameters, based on a desired confidence level. For the whole data analysis part of this thesis, we accept a flat cosmology and therefore $\Omega_\Lambda = 1 - \Omega_m$.

As a first step in our analysis, we are going to use one free model parameter. To this end, we initially take $\mathbf{p} \equiv (\Omega_m)$ for a constant $w = -1$ (ΛCDM) and secondly we use $\mathbf{p} \equiv (w)$ for a constant $\Omega_m = 0.3$ (QDE). We use the distance moduli of 546 SNe I ($z \geq 0.02$) and as the error in eq. (A.4), we take the statistical uncertainty, σ_{stat} that is provided by the *Union2.1* for each SN Ia.

Since we have one fitted parameter, $N_f = 1$, our degrees of freedom will be $d.o.f. = 546 - 1 = 545$. From Table 5 we see that for $N_f = 1$ we have the 1σ (68.3%) confidence level for $\Delta\chi \leq 1$. Also, the 3σ confidence level is provided for $\Delta\chi \leq 9$. The limits within which we search for the best-fit values are $\Omega_m \in [0, 0.65]$ for the density matter and $w \in [-2, -0.5]$ for the DE equation of state parameter. Our typical step sizes are 0.001 for Ω_m and 0.002 for w.

Our results, as shown in Figure 11, are:

- For $w = -1$ (*fixed*):

  $\Omega_m = 0.278^{+0.013}_{-0.014}, \rightarrow \chi^2_{min}/d.o.f. = 520.479/545 = 0.955$

- For $\Omega_m = 0.3$ (*fixed*):

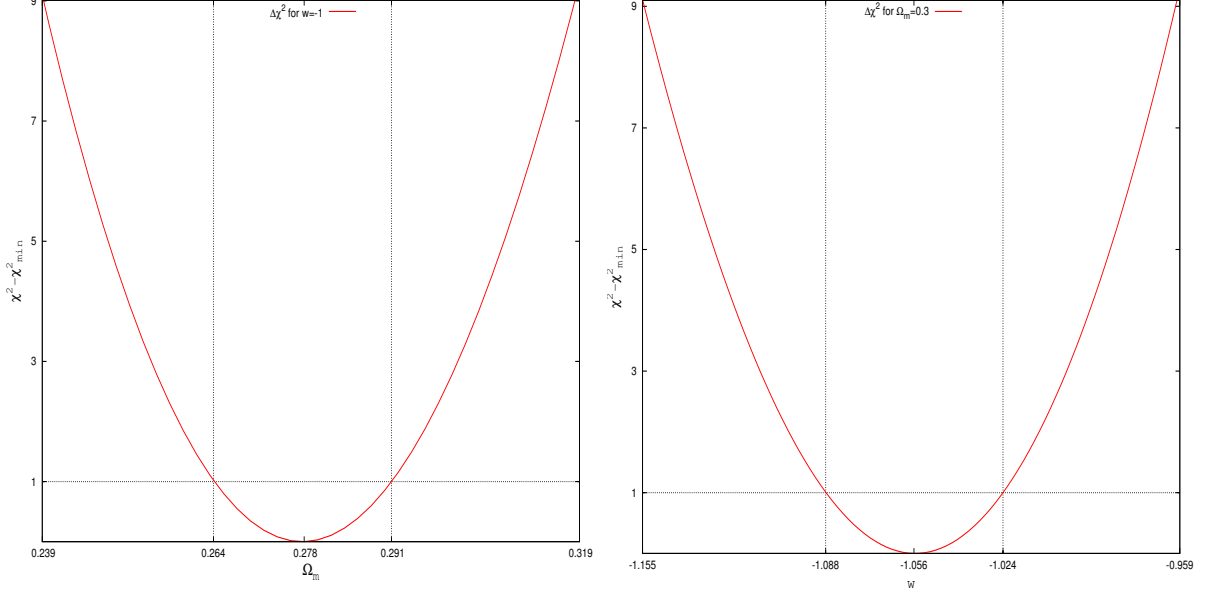 $w = -1.056 \pm 0.032, \rightarrow \chi^2_{min}/d.o.f. = 520.593/545 = 0.955$

Figure 11: *Left panel:* $\Delta\chi^2$ for Ω_m values if $w = -1$ *(fixed).* *Right panel:* $\Delta\chi^2$ for w if $\Omega_m = 0.3$ *(fixed)*

We see that our fit in both cases is excellent, with $\chi^2/d.o.f. = 0.955$. That shows that the best pair of values (w, Ω_m) is very close to these values. Though, it is more efficient to fit both parameters at the same time, as we do later. For the 3σ (99.73%) confidence level ($\Delta\chi^2 \leq 9$), we have $\Omega_m \in [0.239, 0.319]$ and $w \in [-1.154, -0.96]$, limits however that require the second parameter to be fixed a priori.

4.2   One-parameter model (q_0)

We now turn to study the deceleration parameter q_0. For low to medium redshifts, we can use an approximate to eq.(1.8) relation between luminosity distance d_L and q_0,

$$d_L = \frac{c}{H_0}\left[z + \frac{1}{2}(1 - q_0)z^2 + \dots\right] \tag{4.1}$$

Using eq.(4.1) and eq.(1.6) we can again apply the χ^2 minimization analysis and calculate q_0. Since q is a function of time, $q = q(t)$, we have to use redshifts so as $q = q_0$, i.e. the parameter value in our epoch. If we use redshifts, for example, $z > 0.4$, q will not be approximately constant and our calculations would be wrong. We get the SNe Ia with

an increasing z_{max} with a step size of 0.02, in a range of $z \in [0.1, 0.36]$. For every z_{max} we calculate d_L and μ for $q_0 \in [-1.5, 0.5]$ with a step size of 0.001.
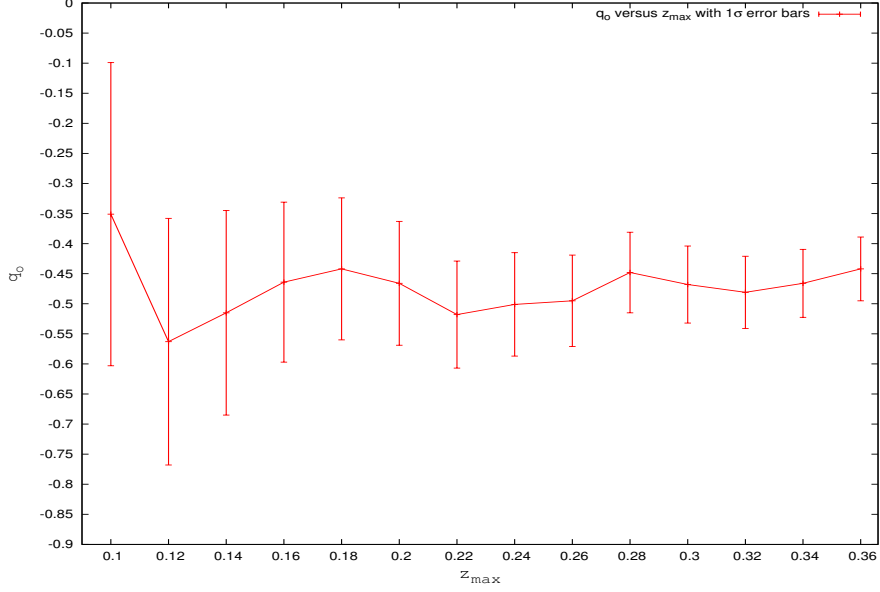

Figure 12: Deceleration parameter q_0 with 1σ error bars versus the maximum redshift z until which we take data

As we can see when we plot our results in Figure 12, there are small differences for different maximum z's. As we increase z_{max}, the 1σ error bars get smaller, because we have more data. For $z_{max} = 0.1$, we have 141 SNe Ia and $q_0 = -0.351^{+0.249}_{-0.252}$ with $\chi^2/d.o.f. = 126.434/140 = 0.903$. These large uncertainties ($\pm71\%$ of the best-fit value) show that we cannot accept a "safe" mean value of q_0. On the other hand, for $z_{max} = 0.24$ we have 218 SNe Ia and $q_0 = -0.501 \pm 0.086$ with $\chi^2/d.o.f. = 204.738/217 = 0.943$. In this case the 1σ uncertainty is much smaller than the previous ($\pm17\%$). This is due to the larger number of data. In both cases, $\chi^2/d.o.f.$ is very satisfying. It is noteworthy that none of the uncertainties limits pass to a positive value of q_0. Every negative value of q_0 corresponds to a positive acceleration of the scale factor, $\ddot{\alpha} > 0$. This indicates that accelerated expansion of our Universe is a robust result even when using limited in z SNe Ia data.

If we accept that $q_0 = -0.501 \pm 0.086$, from the Friedmann equation's (1.1) and their derivatives, eq. (1.2) and eq. (1.4), for a flat Universe ($k = 0$) we have:

$$q_0 = \frac{\Omega_m}{2} - \Omega_\Lambda = -0.501 \Rightarrow$$

$$\frac{\Omega_m}{2} - (1 - \Omega_m) = -0.501 \pm 0.086 \Rightarrow \quad \text{(4.2)}$$

$$\Omega_m = 0.333 \pm 0.057$$

The listed uncertainty has been calculated using error propagation, with $\delta\Omega_m = \frac{2}{3}\delta q_0$ and $\delta q_o = 0.086$. Thus, even if we only use the SNe Ia with $z \leq 0.24$, we have a very good approximation of the matter density Ω_m, consistent with the full QDE model results described below.

4.3 Two-parameter model (Ω_m and w)

The main subject of this thesis is to calculate the best-fit values of the QDE cosmological models, i.e. where $\mathbf{p} \equiv (w, \Omega_m)$, using the reduced χ^2 analysis for a group of SNe Ia data that we choose each time. We also want to plot the solution space within the 1σ uncertainty of our fit and see the limits of the parameters. We use only statistical uncertainties, $\sigma = \sigma_{stat}$, as given in *Union2.1* sample. We accept a QDE model of our Universe.

First, we use the entire sample (546 SNe Ia with $z \geq 0.02$) in order to constrain the two free parameters of the model.

The procedure is as follows: For every w, we use values of the matter density $\Omega_m \in [0, 0.65]$ with a step size of 0.002. When all values of Ω_m are tested for a certain w, we increase w by a step of 0.0025 in a range of $w \in [-2, -0.5]$. Thus, we have $325 \times 600 = 195,000$ different pairs of $\mathbf{p} \equiv (w, \Omega_m)$ to find the best one. For two fitted parameters, $N_f = 2$, the 1σ error corresponds to $\Delta\chi^2 \leq 2.3$ while the 3σ error corresponds to $\Delta\chi^2 \leq 11.83$. We produce a contour plot that shows the best-fit values and the area covered in the w and Ω_m plane for $\Delta\chi^2 \leq 2.3$ and $\Delta\chi^2 \leq 11.83$.

In Figure 13 we show the two contours that correspond to the 1σ and 3σ confidence levels. The corresponding ranges of the 1σ region are: $\Omega_m \in [0.17, 0.364]$ and $w \in [-1.2425, -0.8]$. Moreover, the limits of 99.73% confidence level are: $\Omega_m \in [0, 0.448]$
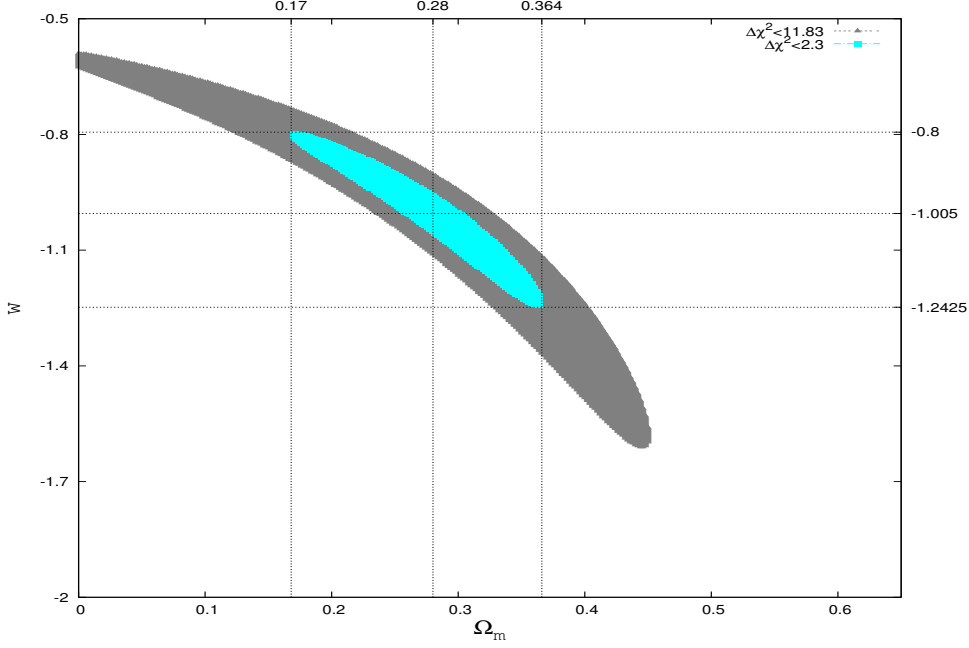
Figure 13: Solution space for w and Ω_m as it occurs from the analysis of the whole sample (546 SNe Ia). The blue contour corresponds to the 1σ confidence level (68.3%) and the grey to the 3σ confidence level (99.73%). The limits of the 1σ confidence level as well as the best-fit values are shown with the dashed lines.

and $w \in [-1.61, -0.59]$. These values may seem to have huge uncertainties but is very important to understand the significance of knowing that there is a possibility of 99.73% for the matter density to be $\Omega_m \leq 0.448$ and the DE equation of state parameter to be $w \geq -1.61$. Of course, not every value of one parameter can be combined with any other value of the second parameter in 1σ limits. For more negative values of w, Ω_m increases and vice versa.

Table 1: QDE cosmology fits for w and Ω_m using all the SNe Ia data (546). When $\mathbf{p} \equiv (w, \Omega_m)$, the uncertainty of each parameter is given by the range for which $\Delta\chi^2 \leq 2.3$ while the other parameter is fixed at its central (best) value.

w	Ω_m	$\chi^2_{min}/d.o.f.$
-1.005 ± 0.045	$0.28^{+0.02}_{-0.018}$	$520.478/544 = 0.956$
$-1\,(fixed)$	$0.278^{+0.013}_{-0.014}$	$520.479/545 = 0.955$
-1.056 ± 0.032	$0.3\,(fixed)$	$520.593/545 = 0.955$

38

The results presented in Table 1 show that our fit is very good, with a reduced $\chi^2_{min} \approx 1$. The extracted values are very common for nowadays cosmology. Furthermore, we see that more data mean lower uncertainties, since for the *Constitution* set (366 SNe Ia with $z \geq 0.02$) the uncertainties are ± 0.053 for w and ± 0.022 for Ω_m (Plionis et al. 2011)

We can visualize our fit results by plotting the distance moduli μ of the SNe Ia versus their redshifts z and using as error bars the σ_{stat}. In the same plot we show the theoretically expected μ versus z for our best-fit model, for a matter dominated, Einstein-de Sitter universe ($w = 0, \Omega_m = 1$) and, for a DE dominated, de Sitter Universe ($w = -1, \Omega_\Lambda = 1$).
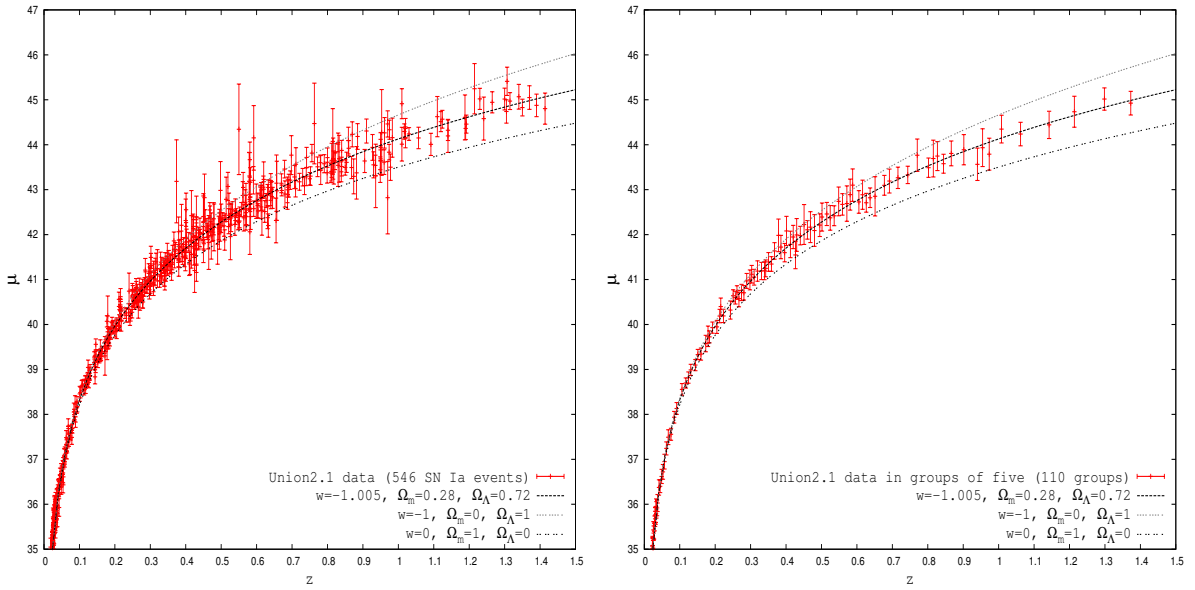

Figure 14: Distance moduli μ as a function of redshift and the expected μ for three cosmological models. *Left panel:* For all SNe Ia (546). *Right panel:* For 108 groups with 5 SNe Ia each and 2 groups with 3 SNe Ia each (the six most distant).

In the left panel of Figure 14 it can be easily seen that our best-fit model describes the data way better than the Einstein-de Sitter model or the matter-empty model. The Einstein-de Sitter model predicts that distant SNe Ia should be brighter by ≈ 0.6 mag at $z \approx 1$ and ≈ 0.7 mag at $z \approx 1.3$ than our best-fit QDE model. Even at $z \approx 0.19$ the deviation of the two models is ≈ 0.2 mag. So, the model that was thought to describe the Universe until 1998 is way off from the observed $\mu - z$ relation. In addition, Figure 14 clearly shows the need of observations of distant SNe Ia in order to obtain the best-fit model with more accuracy.

In the right panel of Figure 14, we group the SNe Ia into groups aggregates in order the tendencies to be more clearly visible. This is realized by sorting the data in ascending redshift order and then group every 5 SNe Ia together, starting from the one with the smallest redshift. The group's μ, z and σ_{stat} are the mean values of the respective quantities of the 5 members of the group. For the last two groups we reduce their membership into 3 SNe Ia per group in order to have a slightly larger dynamical range in z.

4.4   Hubble flow divided in different redshift bins

In order to test whether the solution space of our parameters change, we dissociate our data into three bins. The first one has 272 SNe Ia for $z \in [0.02, 0.314]$. The second and third ones have 137 SNe Ia each and their limits of redshift are $z \in (0.314, 0.57]$ and $z \in (0.57, 1.414]$ respectively. We make the space solution for all three bins in order to find the best-fit values and the 1σ and 3σ confidence levels.

Figure 15 contains some very interesting results. It is obvious that the 1σ contour for $z \in (0.57, 1.414]$ has the lowest uncertainty compared to the two others. This happens due to the fact that high-z SNe Ia are far more important in constraining the cosmological parameters than low-z SNe Ia because the largest model deviations occur at high redshifts, as it is shown in Figure 4. It is interesting to note that although the lowest-z subsample has twice as many SNe Ia as the highest-z subsample, and thus one expects lower random errors, the importance of the high-z regime in constraining the cosmological parameters, as described in Section 3, is the factor that provides the most stringent constraints seen in Figure 15.

However, the size of these contours with respect to the whole sample, are much larger since they contain 1/4 of the data for $z \in (0.314, 0.57]$ and $z \in (0.57, 1.414]$ and relatively low redshifts for the first z-range. The 1σ contour range of the fitted parameter values for the three z-bins are: $w \in [-2, -0.625]$, $\Omega_m \in [0, 0.578]$ for the first shell, $w \in [-2, -0.615]$, $\Omega_m \in [0, 0.54]$ for the second shell and $w \in [-1.665, -0.5575]$, $\Omega_m \in [0, 0.424]$ for the third shell.
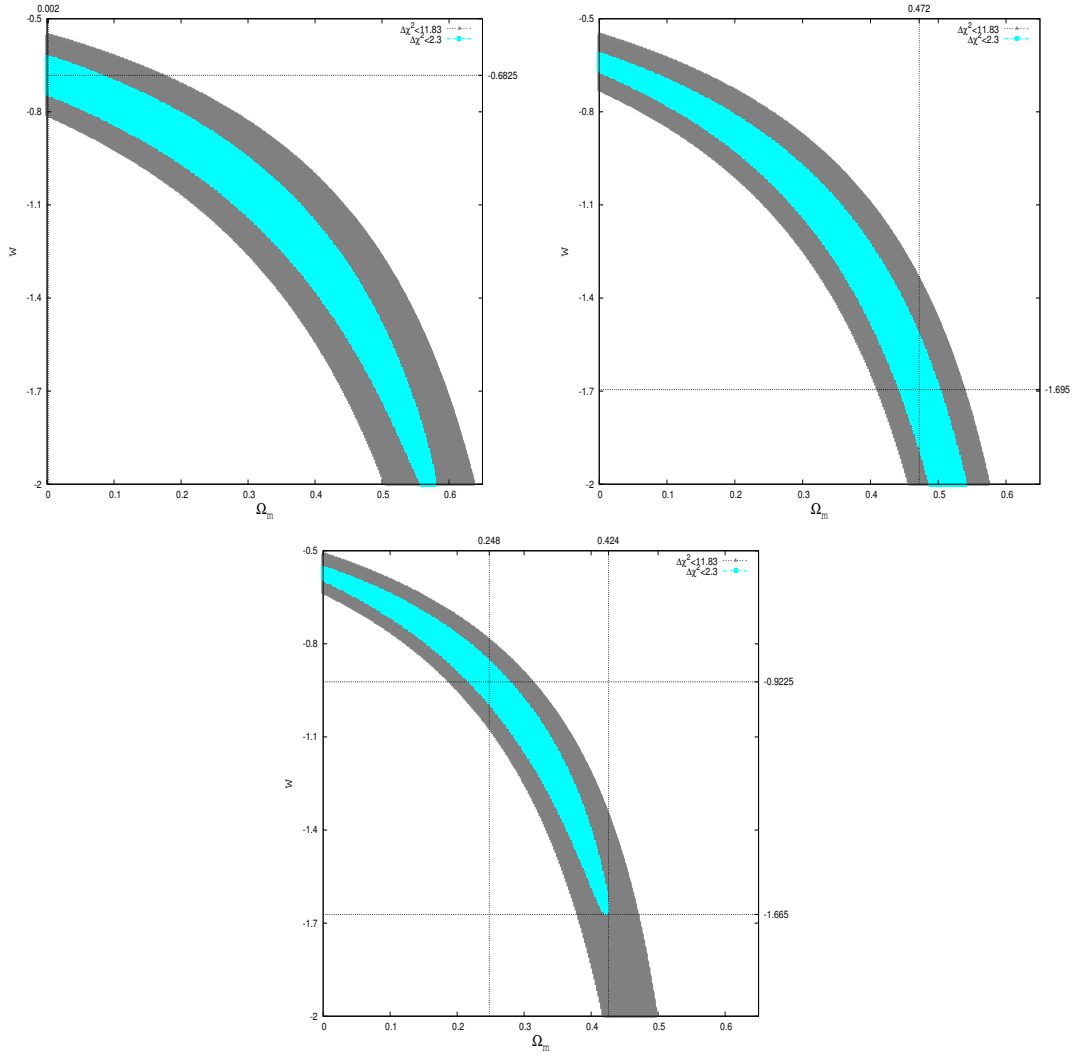
Figure 15: Solution spaces for w and Ω_m The blue contours correspond to the 1σ confidence level (68.3%) and the grey to the 3σ confidence level (99.73%). *Upper left panel:* For the 272 SNe Ia with $z \in [0.02, 0.314]$. *Upper right panel:* For the 137 SNe Ia with $z \in (0.314, 0.57]$. *Bottom center panel:* For the 137 SNe Ia with $z \in (0.57, 1.414]$.

Another interesting fact that is presented in Figure 15 is the variable verticality of the three contour plots. As the redshift increases, the shape of the contours becomes more vertical with respect to the Ω_m-axes and tend to be more parallel to the w-axes. This will be more easily visible in the upcoming sections (Figure 24).

In Table 2 we show the best-fit results and their χ^2_{min} values for the three different z-bins. For the first two bins, our best-fit values of w and Ω_m seem out of the norm. These huge differences between them and the best-fit values from the whole sample should be attributed to the inability to successfully constrain the cosmological parameters when a

41

Table 2: Results of the fits for w and Ω_m using the three redshift's bins SNe Ia data (272, 137 and 137). When $\mathbf{p} \equiv (w, \Omega_m)$, the uncertainty of each parameter is given by the range for which $\Delta \chi^2 \leq 2.3$ when the other parameter is fixed at its central (best) value.

w	Ω_m	$\chi^2_{min}/d.o.f.$
First bin, z $\in$ [0.02, 0.314]		
$-0.6825^{+0.055}_{-0.0725}$	$0.002^{+0.054}_{-0.002}$	$255.352/270 = 0.946$
$-1 \, (fixed)$	$0.275^{+0.054}_{-0.052}$	$255.592/271 = 0.943$
-1.042 ± 0.04	$0.3 \, (fixed)$	$255.639/271 = 0.943$
Second bin, z $\in$ (0.314, 0.57]		
$-1.695^{+0.165}_{-0.1775}$	$0.472^{+0.028}_{-0.026}$	$117.806/135 = 0.873$
$-1 \, (fixed)$	$0.277^{+0.038}_{-0.037}$	$118.07/136 = 0.868$
$-1.052^{+0.082}_{-0.084}$	$0.3 \, (fixed)$	$117.99/136 = 0.868$
Third bin, z $\in$ (0.57, 1.414]		
$-0.9225^{+0.06}_{-0.0625}$	0.248 ± 0.026	$146.761/135 = 1.087$
$-1 \, (fixed)$	0.279 ± 0.026	$146.81/136 = 1.079$
$-1.06^{+0.052}_{-0.054}$	$0.3 \, (fixed)$	$146.905/136 = 1.08$

sample is dominated by low-z, which lead to a huge degeneracy between models. As we explained in the previous sections, all the pairs of $\mathbf{p} \equiv (w, \Omega_m)$ within the 1σ contour plots are of almost equal possibility.

For example, for $z = 0.3$, the deviation in distance modulus for two models $(w, \Omega_m) = (-1.005, 0.28)$ and $(w, \Omega_m) = (-0.6826, 0.002)$, is $\Delta\mu = 0.007$ and for $z = 0.5$ it becomes $\Delta\mu = 0.034$. So, for small samples and low redshifts, models are almost indistinguishable,

thus all the combinations of w and Ω_m inside the 1σ contour are equally possible.

In order to test how much the SNe Ia with intermediate redshifts affect the final space solution, we produce the 1σ and 3σ contour plots without the medium redshift bin which has $z \in (0.314, 0.57]$ and contains 137 SNe Ia and we compare it with the solution space that occurs from the analysis of the whole sample.
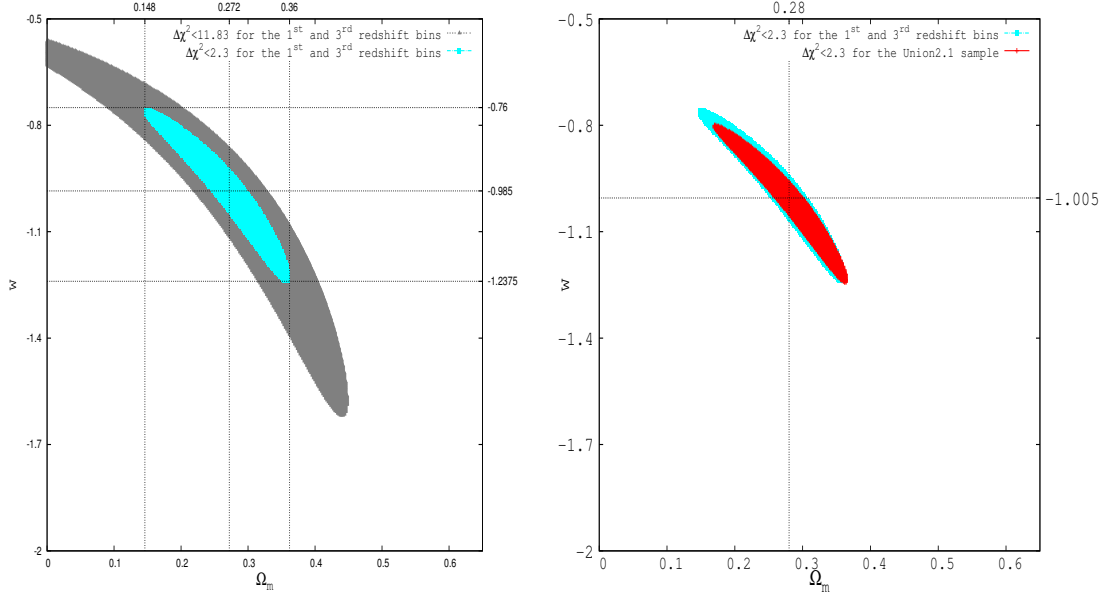

Figure 16: Solution spaces for w and Ω_m. *Left panel:* The blue contour corresponds to the 1σ confidence level (68.3%) and the grey to the 3σ confidence level (99.73%) for the 409 SNe Ia of the 1st and 3rd redshift bins. *Right panel:* 1σ contours for the whole *Union2.1* sample (red contour) and for the 409 SNe Ia from the 1st and 3rd redshift bins.

As we can see in Figure 16, in this case the resulting solution space is almost identical with that of the whole sample. It causes just a small shift of the best-fit parameter values (2.86% for Ω_m, 2% for w) and slightly larger 1σ contours of the parameters. Specifically we can compare the two solutions below:

- For the joint 1st and 3rd redshift bins:

$$w = -0.985^{+0.0525}_{-0.055} \qquad , \qquad \Omega_m = 0.272 \pm 0.022 \qquad \text{with}$$

$$\chi^2_{min}/d.o.f. = 402.398/407 = 0.989 \quad \text{with } 1\sigma \text{ corresponding ranges, } w \in [-1.2375, -0.76],$$

$$\Omega_m \in [0.148, 0.36]$$

- For the whole sample:

$$w = -1.005 \pm 0.045 \qquad , \quad \Omega_m = 0.28^{+0.02}_{-0.018} \qquad \text{with}$$

$$\chi^2_{min}/d.o.f. = 520.478/544 = 0.956 \quad \text{with } 1\sigma \text{ corresponding ranges, } w \in [-1.2425, -0.8],$$

$$\Omega_m \in [0.17, 0.364]$$

This probably implies that it is more efficient for future surveys to focus on observing only low and relatively high redshift standard candles while omitting intermediate redshifts.

5 Investigating possible Hubble expansion anisotropies

5.1 Among the two galactic hemispheres

In order to test if there is any anisotropy in expansion between the two galactic hemispheres, we perform the same work as above for each hemisphere separately. First present the redshift distribution of their data.

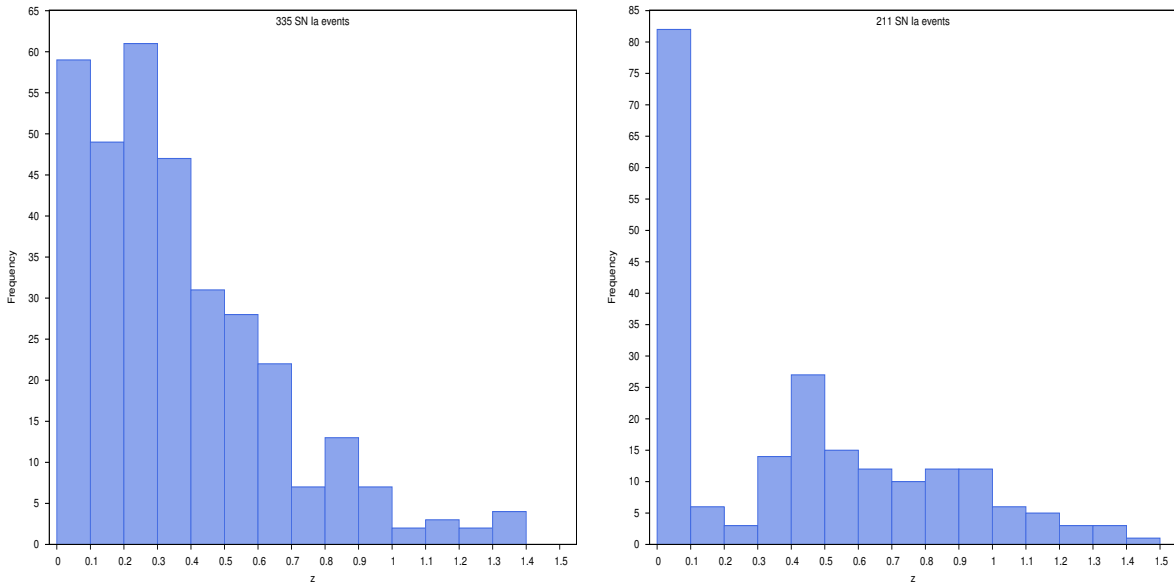**Figure 17:** Redshift distribution of the SNe Ia with $z \geq 0.02$. *Left panel:* Southern galactic hemisphere ($b < 0$, 335 SN Ia events) *Right panel:* Northern galactic hemisphere ($b > 0$, 211 SN Ia events).

Figure 17 shows us that the redshift distributions of the two galactic hemispheres are quite distinct. The data of the southern galactic hemisphere are more normally distributed while in the northern galactic hemisphere there are 82 SNe Ia (39% of the total) with $z < 0.1$ and only 9 SNe Ia with $0.1 \leq z < 0.3$. This can make the differentiation of the fitting cosmological models even harder in the northern galactic hemisphere. This is because for low redshifts, distance moduli deviations $\Delta\mu$ between the models are very small to distinguish and much smaller than the statistical uncertainties. For example, at $z = 0.3$ for two models $(w, \Omega_m) = (-0.6, 0)$ and $(w, \Omega_m) = (-2, 0.6)$ we have $\Delta\mu = 0.01$. On the other hand, the two galactic hemispheres have similar number of SNe Ia for $z \geq 0.4$, 119 for the southern and 106 for the northern.

We follow the same procedure as for the whole sample, in order to calculate the best-fit values for $\mathbf{p} \equiv (w, \Omega_m)$ for each galactic hemispheres. The grids,the contour plots and the typical step size are the same with the whole sample's analysis.
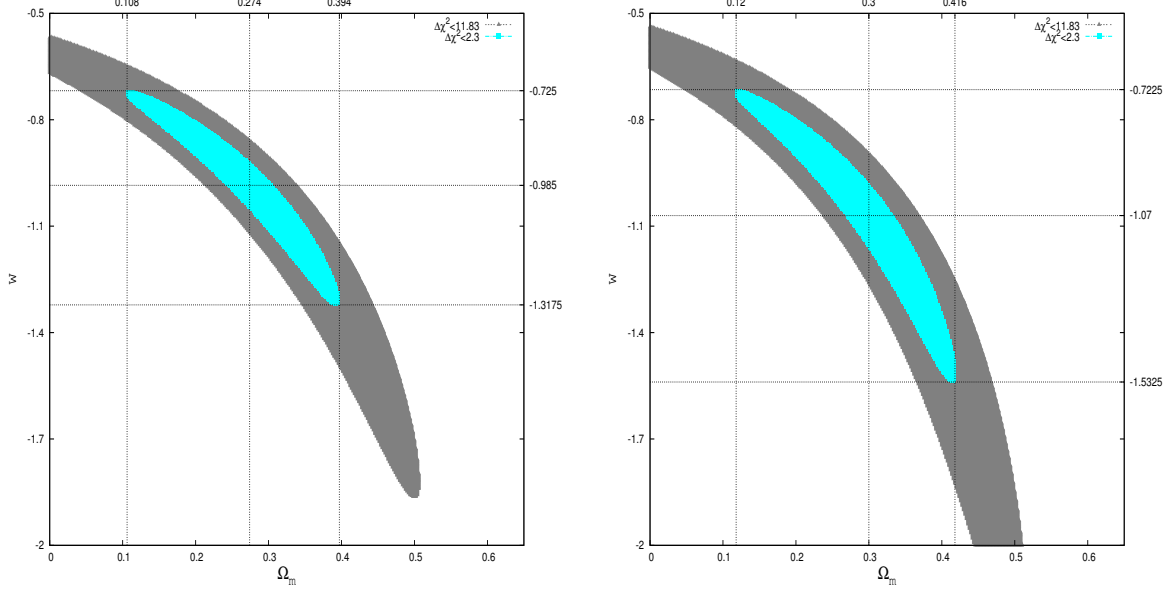

Figure 18: Solution spaces for w and Ω_m. The blue contours correspond to the 1σ confidence level (68.3%) and the grey to the 3σ confidence level (99.73%). *Left panel:* For the 335 SNe Ia of the southern galactic hemisphere. *Right panel:* For the 211 SNe Ia of the northern galactic hemisphere.

In Figure 18 the corresponding ranges of 1σ contour for the southern galactic hemisphere are $\Omega_m \in [0.108, 0.394], w \in [-1.3175, -0.725]$ and for the northern are $\Omega_m \in [0.12, 0.416], w \in [-1.5325, -0.7225]$. These constraints of parameters, as expected, are somewhat larger than the constraints from the whole sample. As the amount of data increases, the uncertainties decrease. The 1σ contour of the whole sample is a subset of the respective contours of the two hemispheres.

In Table 3 we present the results of the χ^2_{min} analysis for the southern and northern hemisphere.

It can be seen that the best-fit values for the two hemispheres are slightly different but within the 1σ uncertainty contours range. Both hemispheres' solution spaces contain the best-fit parameter values of the whole sample, as seen in Table 1. The value of $\chi^2_{min}/d.o.f.$ is very close to unity, especially for the southern galactic hemisphere.

Table 3: Results of fits for w and Ω_m using independently the southern and northern galactic hemispheres' SNe Ia data (335 and 211 respectively). When $\mathbf{p} \equiv (w, \Omega_m)$, the uncertainty of each parameter is the range for which $\Delta \chi^2 \leq 2.3$ when the other parameter is fixed at its central (best) value.

w	Ω_m	$\chi^2_{min}/d.o.f.$
Southern galactic hemisphere		
-0.985 ± 0.0575	$0.274^{+0.026}_{-0.028}$	$334.588/333 = 1.005$
$-1 \, (fixed)$	0.28 ± 0.02	$334.594/334 = 1.002$
-1.0425 ± 0.04	$0.3 \, (fixed)$	$334.664/334 = 1.002$
Northern galactic hemisphere		
-1.07 ± 0.08	$0.3^{+0.03}_{-0.028}$	$185.741/209 = 0.889$
$-1 \, (fixed)$	0.274 ± 0.02	$185.817/210 = 0.885$
$-1.07^{+0.052}_{-0.054}$	$0.3 \, (fixed)$	$185.741/210 = 0.884$

As we did for the whole sample, we plot the distance moduli μ with the statistical uncertainties σ_{stat} versus the redshift of the SNe Ia for each hemisphere as well as the best-fit models. Moreover, we plot the theoretical distance modulus expectations for the Einstein-de Sitter and the de Sitter model.

In Figure 19 we see that the best-fit model for each hemisphere predicts almost the same μ with the best-fit model of the whole sample for $z < 1.5$. In addition, the lack of data for $0.1 \leq z < 0.3$ in the northern galactic hemisphere is characteristic. Finally, the northern data contain more "outliers", since the SNe Ia in redshifts $z = 0.375, 0.55, 0.592$ deviate from the best-fit model by 3.98%, 4.25% and 3.33% respectively. Also, the first two have the two largest statistical errors of the whole sample ($\sigma_{stat} = 0.9232$ and $\sigma_{stat} = 1.006$ respectively) and the third one has the fourth largest error ($\sigma_{stat} = 0.718$). The third largest error of the sample belongs to the SN Ia at $z = 0.97$ of the northern galactic
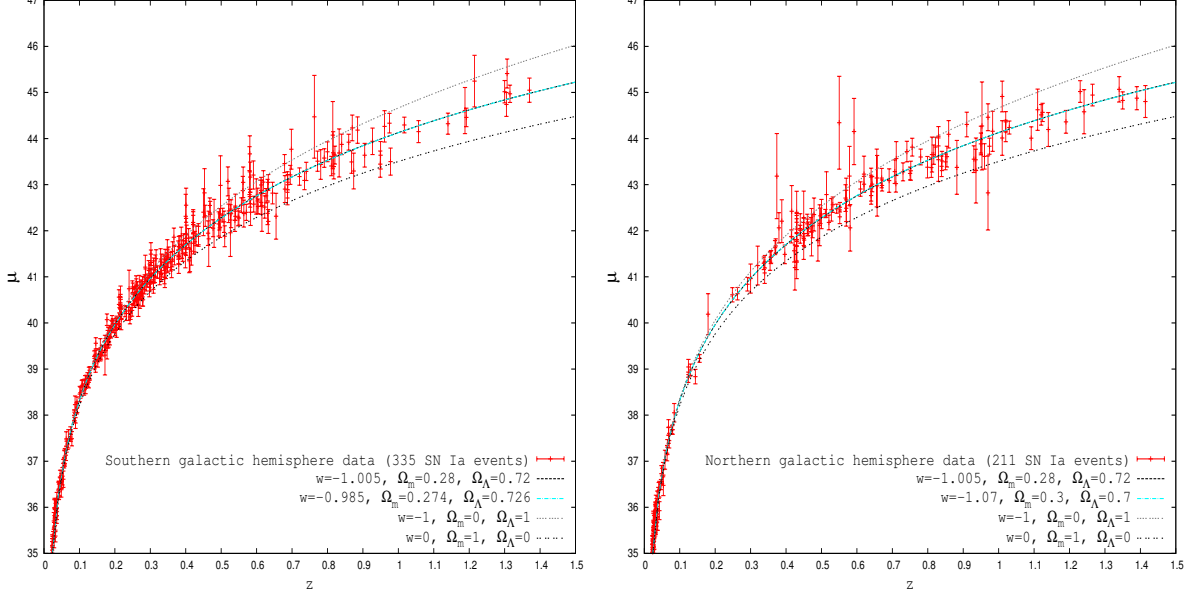
Figure 19: SNe Ia distance moduli μ as a function of redshift and the expected μ for four cosmological models. *Left panel:* The southern galactic hemisphere's 335 SNe Ia *Right panel:* The northern galactic hemisphere's 211 SNe Ia.

hemisphere again, which deviates from the best-fit model by 2.8%.

5.2   Among random groups of SNe Ia

In order to test further if there are any anisotropies in the Hubble expansion, we select four solid angles that contain SNe Ia spanning a large dynamical range in redshift. Two of them are in the southern galactic hemisphere and the other two in the northern. These groups are:

- Group A with $l \in [160, 185]$ and $b \in [-63, -50]$ which contains 82 SNe Ia

- Group B with $l \in [50, 80]$ and $b \in [-70, -38]$ which contains 53 SNe Ia

- Group C with $l \in [160, 220]$ and $b \in [10, 60]$ which contains 46 SNe Ia

- Group D with $l \in [85, 140]$ and $b \in [45, 70]$ which contains 63 SNe Ia

In Figure 20 we present the results of the usual χ^2-minimization procedure. We have used the same step in Ω_m and w as before.
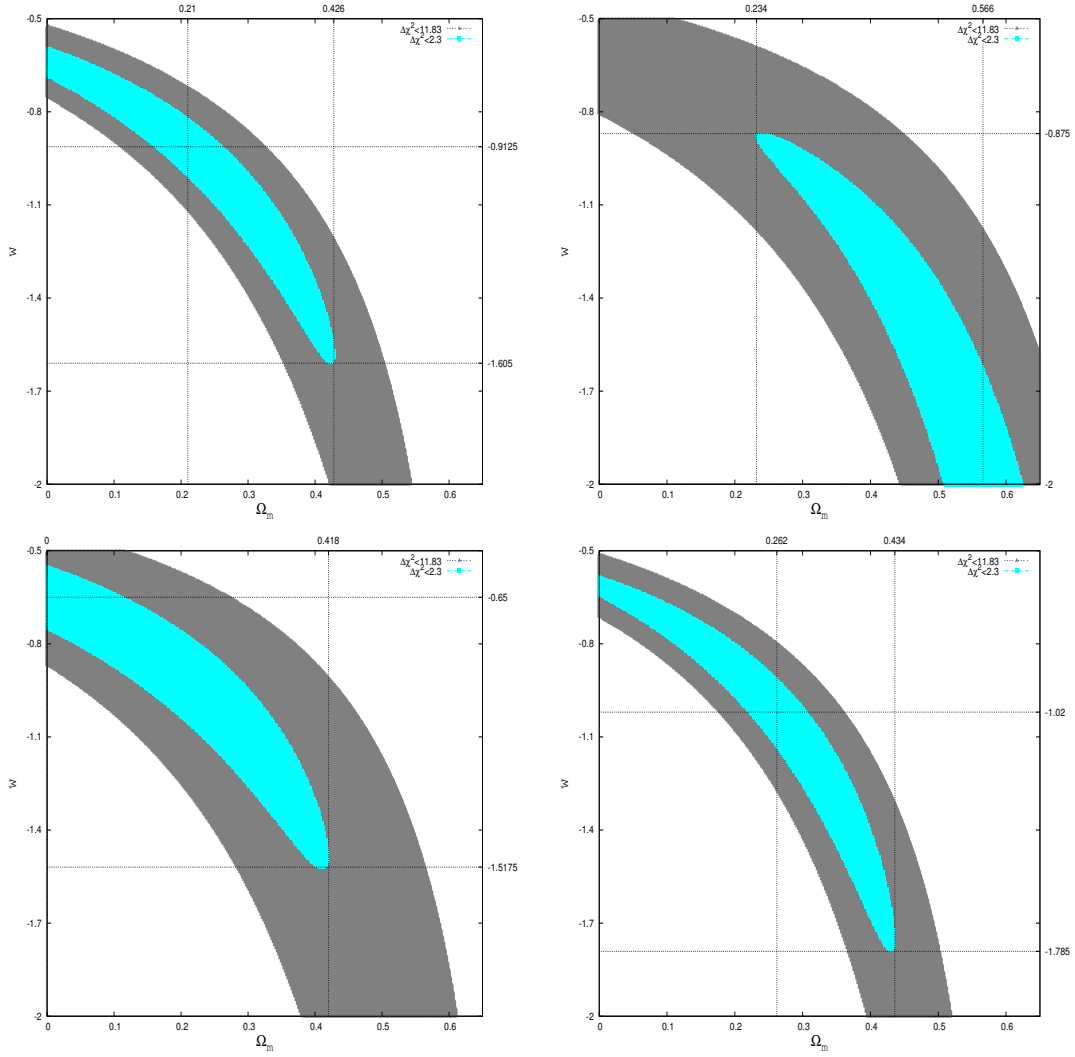
Figure 20: Solution space for w and Ω_m. The blue contour corresponds to the 1σ confidence level (68.3%) and the grey to the 3σ confidence level (99.73%). *Upper left panel:* As it occurs from Group A (82 SNe Ia). *Upper right panel:* As it occurs from Group B (53 SNe Ia). *Bottom left panel:* As it occurs from Group C (46 SNe Ia). *Bottom right panel:* As it occurs from Group D (63 SNe Ia).

We see that for Group B and Group C the 1σ contours seem very different since they had totally different best-fit values of w and Ω_m. Although we have significantly fewer data for each group than we had for the first redshift shell, $z \in [0.02, 0.314]$, the uncertainties in Group A and Group D are lower. This is a result of the variety of redshifts in these groups as we see below. Specifically, the corresponding ranges of 1σ contours of these groups are:

- Group A: $w \in [-1.605, -0.5975]$, $\Omega_m \in [0, 0.426]$

- Group B: $w \in [-2, -0.875]$, $\Omega_m \in [0.234, 0.622]$

- Group C: $w \in [-1.5175, -0.555]$, $\Omega_m \in [0, 0.418]$

- Group D: $w \in [-1.785, -0.5875]$, $\Omega_m \in [0, 0.434]$

Groups C which has the fewest data, also has the lowest 1σ corresponding range for w, while its uncertainty for Ω_m for every value of w is the highest.

In Table 4 we summarize the results of χ^2 analysis for the four data Groups. It is noteworthy that Groups A and D provide results very near to those of the whole SNe Ia sample, and they also have the lowest $\chi^2/d.o.f.$. Of course, they have the most SNe Ia compared with the other groups. Even more important is that they also have high-z data unlike Groups B and C. There is one more interesting observation and is that for Group B, χ^2 for $(w, \Omega_m) = (-1, 0.312)$ has an important deviation of the best-fit values, $\Delta\chi^2 = 1.88$. There is no other deviation as large as this for $w = -1 \, (fixed)$ from χ^2_{min} in this thesis for any other group of data. This may be a hint for a small anisotropy in the expansion of the Universe for these coordinates, something that we analyse in the next chapter. In order to see the best-fit models with the corresponding data we produce the μ vs.z plots for each group.

In Figure 21 we plot the SNe Ia distance moduli μ as a function of redshift z of each Group. We also plot the best-fit model as it occurs for each Group, the best-fit model for the whole sample $(w, \Omega_m) = (-1.005, 0.28)$, the Einstein-de Sitter model and the de Sitter model. It is evident that Groups A and D have several high-z SNe Ia $(z \geq 1)$, while they lack in Groups B and C, with the highest redshift of Group B being $z = 0.687$ and of Group C being $z = 0.882$.

In addition, for Groups B and C, the value of $\chi^2_{min}/d.o.f.$ indicates that the fitted model is not such a good fit to the data. The main characteristic of Group C is that it contains the four SNe Ia with the largest uncertainties. The deviations of these distance moduli $\Delta\mu$ from the theoretically expected μ_{th} are quite large. For example, the SN1997l with $z = 0.55$ have a deviation of the best-fitted model of $\Delta\mu = 1.795 \, mag$ with an uncertainty of $\sigma_\mu = 1.006$. Even for the de Sitter model $(w = -1, \Omega_\Lambda = 1)$ it has $\Delta\mu = 1.53 \, mag$. If

Table 4: Complete table of fits for w and Ω_m using Group A,B,C and D SNe Ia data (82, 53, 46 and 63 respectively). When $\mathbf{p} \equiv (w, \Omega_m)$, the uncertainty of each parameter is the range for which $\Delta\chi^2 \leq 2.3$ when the other parameter is fixed at its central (best) value.

| w	Ω_m	$\chi^2_{min}/d.o.f.$
Group A, $\mathbf{l} \in [\mathbf{160}, \mathbf{185}], \mathbf{b} \in [\mathbf{-63}, \mathbf{-50}]$		
$-0.9125^{+0.085}_{-0.0875}$	$0.21^{+0.048}_{-0.044}$	$64.6/80 = 0.808$
$-1\,(fixed)$	0.253 ± 0.044	$64.66/81 = 0.798$
-1.11 ± 0.04	$0.3\,(fixed)$	$65.879/81 = 0.813$
Group B, $\mathbf{l} \in [\mathbf{50}, \mathbf{80}], \mathbf{b} \in [\mathbf{-70}, \mathbf{-38}]$		
$-2^{+0.366}$	0.566 ± 0.054	$60.02/51 = 1.177$
$-1\,(fixed)$	$0.312^{+0.09}_{-0.085}$	$61.9/52 = 1.19$
-0.996 ± 0.0168	$0.3\,(fixed)$	$61.938/52 = 1.214$
Group C, $\mathbf{l} \in [\mathbf{160}, \mathbf{220}], \mathbf{b} \in [\mathbf{10}, \mathbf{60}]$		
-0.65 ± 0.095	$0^{+0.108}$	$49.52/44 = 1.125$
$-1\,(fixed)$	$0.248^{+0.088}_{-0.079}$	$50.3/45 = 1.12$
$-1.096^{+0.16}_{-0.214}$	$0.3\,(fixed)$	$50.6/45 = 1.127$
Group D, $\mathbf{l} \in [\mathbf{85}, \mathbf{140}], \mathbf{b} \in [\mathbf{45}, \mathbf{70}]$		
-1.02 ± 0.095	$0.262^{+0.042}_{-0.039}$	$54.779/61 = 0.898$
$-1\,(fixed)$	$0.257^{+0.043}_{-0.039}$	$48.023/62 = 0.775$
$-1.116^{+0.118}_{-0.126}$	$0.3\,(fixed)$	$48.09/62 = 0.776$
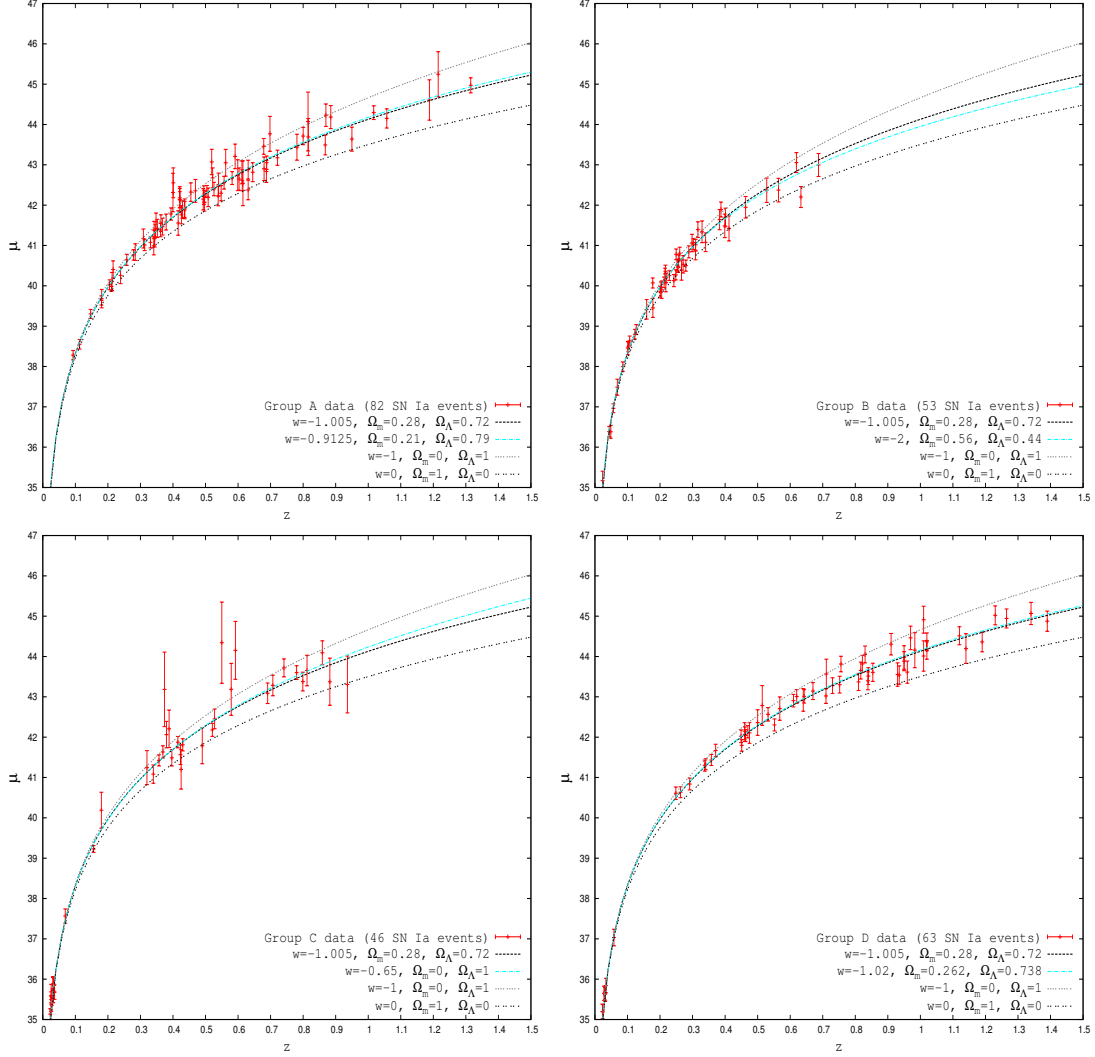
Figure 21: Distance moduli μ as a function of redshift and expected μ for four cosmological models. *Upper left panel:* Group A (82 SNe Ia) *Upper right panel:* Group B (53 SNe Ia). *Bottom left panel:* Group C (46 SNe Ia). *Bottom right panel:* Group D (63 SNe Ia).

we take into account the other "outliers" of this Group as well we can explain why we have such a high value of $\chi^2_{min}/d.o.f.$ for Group C. On the other hand, the data of Group B do not seem to have "outliers" and they generally have small uncertainties. But that exactly is the reason of the high value of $\chi^2_{min}/d.o.f.$ and the apparently bad fit. The low values of the uncertainties, being in the denominator of eq. (A.4), do not allow significant deviations of the data from the model. This means that even for a very good fit to the data, if two or three SNe Ia have a deviation of $\Delta\mu \approx \sigma_\mu$ the χ^2 value rises, resulting in this case to a $\chi^2_{min}/d.o.f. = 1.177$.

For the Groups A and D, the fit of the data are quite satisfying. Especially for Group D, the best-fit values are very close to the best-fit model from the whole sample, $(w, \Omega_m) = (-1.005, 0.28)$. Furthermore, the deviations of distance moduli of the models for these Groups compared to those from the whole sample, are very small even for $z = 1.5$ (for Group D, $\Delta\mu = 0.038$). In contrast, the deviations $\Delta\mu$ for the best-fit models to the data of Groups B and C are larger at high redshifts ($\Delta\mu = -0.26$ and $\Delta\mu = 0.223$ for $z = 1.5$ respectively) but insignificant at the redshift range covered by the data. If there is any anisotropy in the expansion of the Universe for these directions, it is not easily seen, although the results based on Group B ($l \in [50, 80]$ and $b \in [-70, -38]$) have the most distinct 1σ contour in the Ω_m-w place with respect to all the other Groups.

To find out if this peculiarity of the solution space of Group B is a result of the low-z data, we also find the solution space for the data of Group A but for the same upper-z limit ($z \leq 0.689$). We also find the solution space for the whole *Union2.1* sample after limiting its redshift to the same upper-z limit ($z \leq 0.689$).

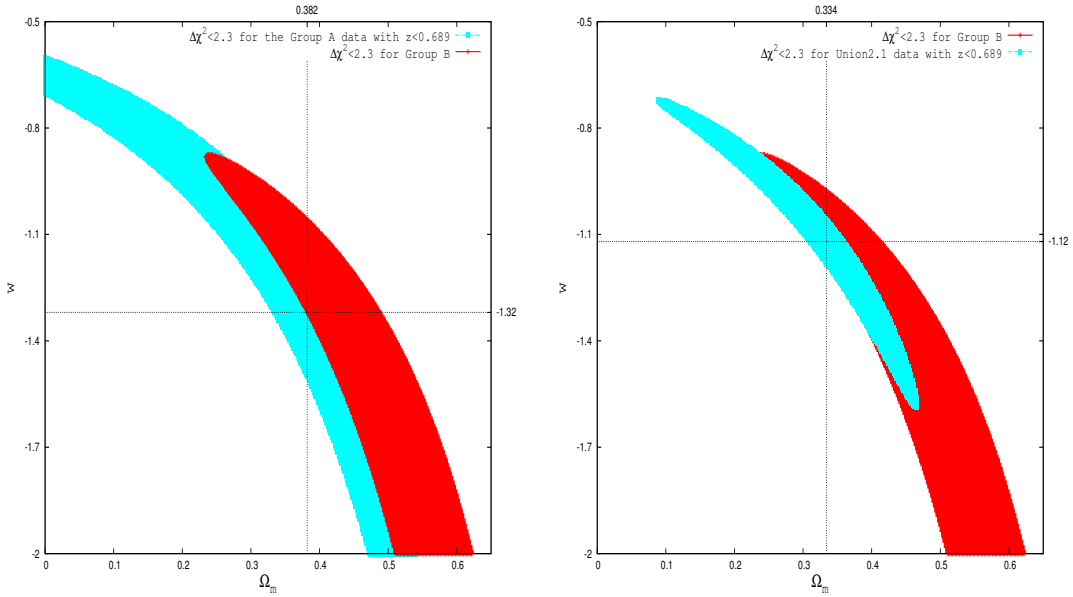**Figure 22:** 1σ contour plots of the Ω_m-w plane. *Left panel:* As they occur from data from Group A with $z \leq 0.689$ (blue contour, 67 SNe Ia) and Group B (red contour, 53 SNe Ia). *Right panel:* As they occur from *Union2.1* with $z \leq 0.689$ (blue contour, 453 SNe Ia) and Group B (red contour, 53 SNe Ia).

In Figure 22 we see that if we use only the data with $z \leq 0.689$, the best-fit values come closer to those of Group B than before. For clarity, we use only the 1σ contour plots. For Group A, we have $(w, \Omega_m) = (-1.32, 0.382)$ with $\chi^2_{min}/d.o.f. = /65 =$ and for *Union2.1* we have $(w, \Omega_m) = (-1.12, 0.334)$ with $\chi^2_{min}/d.o.f. = 427.433/451 = 0.948$. Although there is a significant overlapping between the 1σ contours, especially for Group A, the difference of the solution space for the same maximum redshift appears still important. Thus, constraining the upper redshift limit brings the results based on Group B closer to those of Group A and of the whole sample but still there is significant discrepancies.

6 Joint likelihood analysis

Once we have the solution spaces for several independent groups of SNe Ia, we can use them to perform a joint likelihood analysis and compare the extracted results with those from the χ^2 analysis from the whole sample.

6.1 Joint likelihood analysis for the two galactic hemispheres

First we consider the southern and the northern galactic hemispheres' distance moduli as our two independent groups of data.
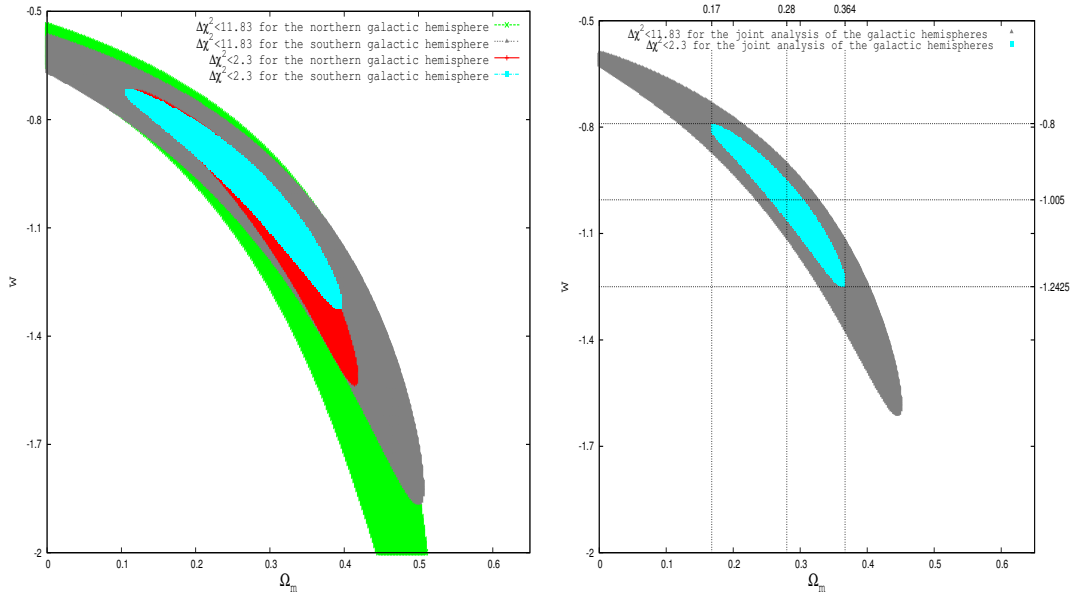

Figure 23: *Left panel:* 1σ and 3σ contour plots of southern (blue and grey contours) and northern (red and green contours) galactic hemispheres. *Right panel:* Solution space for w and Ω_m as it occurs from the joint likelihood analysis for the two galactic hemispheres. The blue contour corresponds to the 1σ confidence level (68.3%) and the grey to the 3σ confidence level (99.73%)

As we can see in the left panel of Figure 23, the contours of the southern galactic hemisphere are smaller and less vertical with respect to the Ω_m-axes than the corresponding northern ones. The joint analysis of the two hemispheres provides $\chi^2_{min}/d.o.f. = 520.478/(333 + 209) = 0.96$ for $(w, \Omega_m) = (-1.005, 0.28)$. In the right panel of Figure 23 we have the solution space as it occurs from the joint analysis. As expected, the best-fit

values, the corresponding ranges of 1σ and 3σ contours as well as the value of χ^2_{min} are *exactly* the same with these from the full sample analysis. The only difference is that the *d.o.f.* are reduced and the $\chi^2_{min}/d.o.f.$ is closer to unity than before.

6.2 Joint likelihood analysis for the three redshift bins

The next subdivisions of the sample that we are going to use are the three redshift bins as they defined before. The first bin contains 272 SNe Ia for $z \in [0.02, 0.314]$, the second contains 137 SNe Ia for $z \in (0.314, 0.57]$ and finally the third also contains 137 SNe Ia, for $z \in (0.57, 1.414]$.
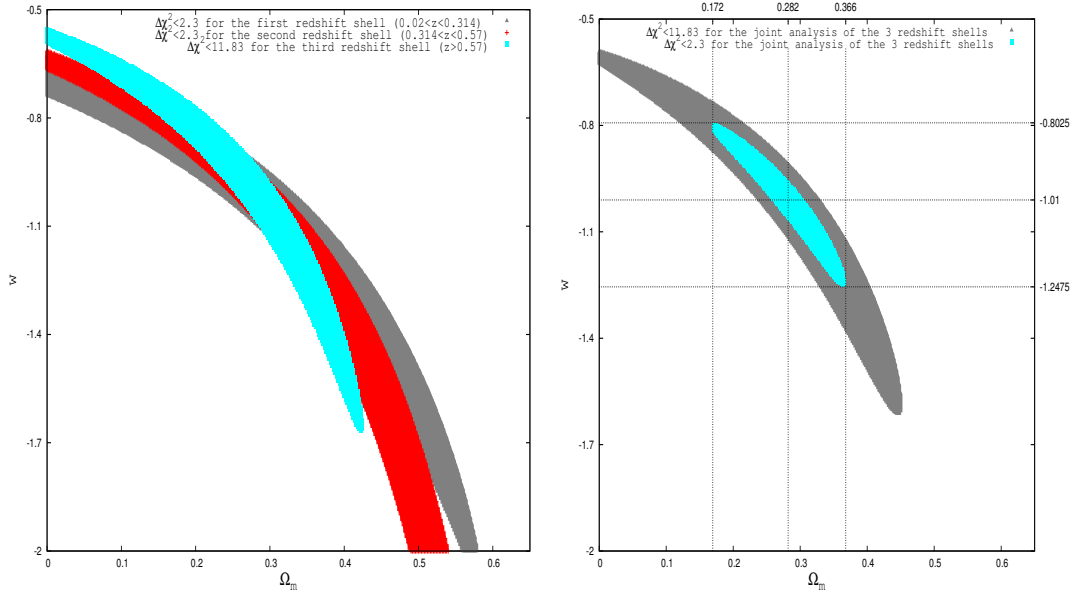

Figure 24: *Left panel:* 1σ contour plots of the three redshift bins (for clarity we do not plot any other contours). *Right panel:* Solution space for w and Ω_m as it occurs from the joint likelihood analysis for the three redshift bins. The blue contour corresponds to the 1σ confidence level (68.3%) and the grey to the 3σ confidence level (99.73%)

From this joint analysis, the results are *slightly* different from those from the whole sample due to round-up errors. The values with the lowest χ^2 are $(w, \Omega_m) = (-1.01, 0.282)$ with $\chi^2_{min}/d.o.f. = 520.735/(270 + 135 + 135) = 0.964$. The best-fits values and the uncertainties of them when one parameter is fixed are the same with these from the whole sample. The best-fit combination for the whole sample $(w, \Omega_m) = (-1.005, 0.28)$

have a deviation of $\Delta \chi^2 = 6.6 \times 10^{-4}$, being almost an equally good fit that is extracted by the joint analysis. Indeed, it is the combination with the lowest $\Delta \chi^2$ of all.

As we mentioned before for higher redshifts the corresponding contours are more vertical to the Ω_m-axes. Also, we see more clearly that the third and more distant redshift bin provides the smallest size contour region, although has half the data of the first bin. This is an excellent indication of the importance of the high-z data.

6.3 Joint likelihood analysis of ten independent SNe Ia subsamples

In order to identify possible anisotropies of the Hubble expansion, we now divide the *Union2.1* sample in 10 fully independent SNe Ia subsamples. Except for the Groups A,B,C and D we also have:

- Group E with $l \in [245, 360]$ and $b \in [10, 80]$ with 56 SNe Ia

- Group F with $l \in [90, 158]$ and $b \in [-70, -50]$ with 68 SNe Ia

- Group G with $l \in [25, 80]$ and $b \in [-35, 90]$ with 47 SNe Ia

- Group H with $l \in [81, 215]$ and $b \in [-50, -5]$ which contains 54 SNe Ia

- Group K with $l \in [30, 45,]$ and $b \in [-90, -40]$ with 22 SNe Ia

- Group M with all the remaining 55 SNe Ia

We do not use letters "I, J, L" because they can be mistaken with "1" and with each other. Group K has the fewest data but it has important, high-z data with a mean redshift of $\overline{z} = 0.6847$.

In section 5 we pointed out the peculiarity of the solution space provided by Group B. Since Group K is very near to Group B in galactic coordinates (Figure 9), we join the two Groups (B and K) in one group and calculate again the solution space of w and Ω_m. The area of these groups in celestial coordinates is between $\alpha \in [21.2^h, 23.94^h]$ and $\delta \in [-26.36^o, 13.46^o]$. We have to mention here that Group K alone gives similar best-fit

values ($w = -2, \Omega_m = 0.51$) with Group B and the fact that it has the closest coordinates to Group B is a strong hint for a consistent behaviour of this whole region.

The best-fit values of the cosmological parameters provided by the joint B+K subsample are $w = -1.7025^{+0.25}_{-0.275}$ and $\Omega_m = 0.498^{+0.042}_{-0.04}$ while the 1σ ranges are: $w \in [-2, -0.8825]$ and $\Omega \in [0.262, 0.574]$. However due to the degeneracy of the solution, the best-fit parameters of the whole SNe Ia sample are not included within the 1σ contour provided by the B+K group.

When we exclude every other Group from the whole sample, the solution spaces does not change significantly. This means that the 1σ contours for all Groups except for B and K, are consistent with the results of the rest of the data.

7 Further analysis for the unusual sky region

Since we identified this sky region with a distinctly different $(w$-$\Omega_m)$ solution with respect to all other regions of the sky and of the whole sample together, we now slightly expand the subsample to include all SNe Ia in this part of the sky, which is limited by the following galactic coordinates:

$$35^o < l < 83^o$$

$$-79^o < b < -37^o$$

This sky region, which we call Group X, contains 82 SNe Ia (7 more than Groups B+K). Performing the usual χ^2_{min} minimization procedure, we find the best-fit values for Group X and plot the 1σ contour plot, to be compared with the 1σ contour plot of the rest of the SNe Ia.
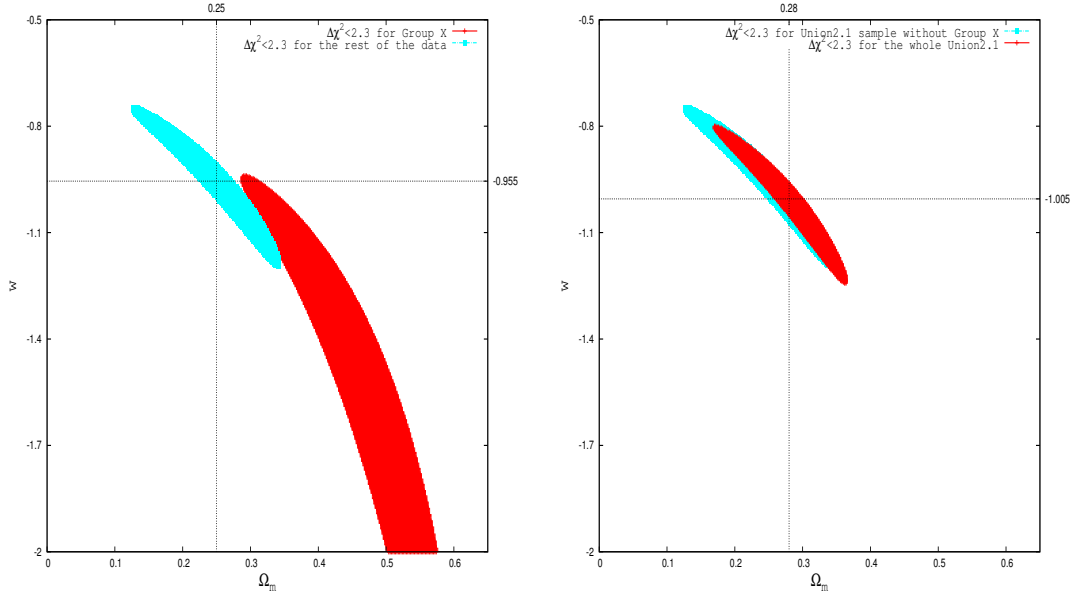

Figure 25: *Left panel:* 1σ contour plots of Group X (red contour) and for the rest of the data (blue contour). *Right panel:* 1σ contour plots for the whole *Union2.1* sample (red contour) and for the sample without Group X (blue contour).

- For Group X:

$$w = -1.74^{+0.245}_{-0.26} \quad , \quad \Omega_m = 0.504^{+0.04}_{-0.038} \quad \text{with}$$

$$\chi^2_{min}/d.o.f. = 91.203/80 = 1.14 \quad \text{with } 1\sigma \text{ corresponding ranges, } w \in [-2, -0.94] \,,$$

59

$\Omega_m \in [0.288, 0.574]$

- For the rest of the data:

$$w = -0.955 \pm 0.045 \qquad , \qquad \Omega_m = 0.25^{+0.022}_{-0.02} \qquad \text{with}$$

$$\chi^2_{min}/d.o.f. = 425.528/462 = 0.92 \quad \text{with } 1\sigma \text{ corresponding ranges, } w \in [-1.195, -0.7475],$$

$$\Omega_m \in [0.126, 0.342]$$

As we see in the left panel of Figure 25 the 1σ contour plot of the Group X data is significantly different than that of the rest of the sample with the two contours having nearly no common solution space. In the right panel, there is a 5.2% change in the best-fit w value and a 12% change in the best fit Ω_m value when we use all the data compared with the case where we exclude Group X from the analysis. The shift in the Ω_m best-fit value is quite important since it indicates that the amount of matter in the Universe, may be overestimated because of the behaviour of Group X SNe Ia.
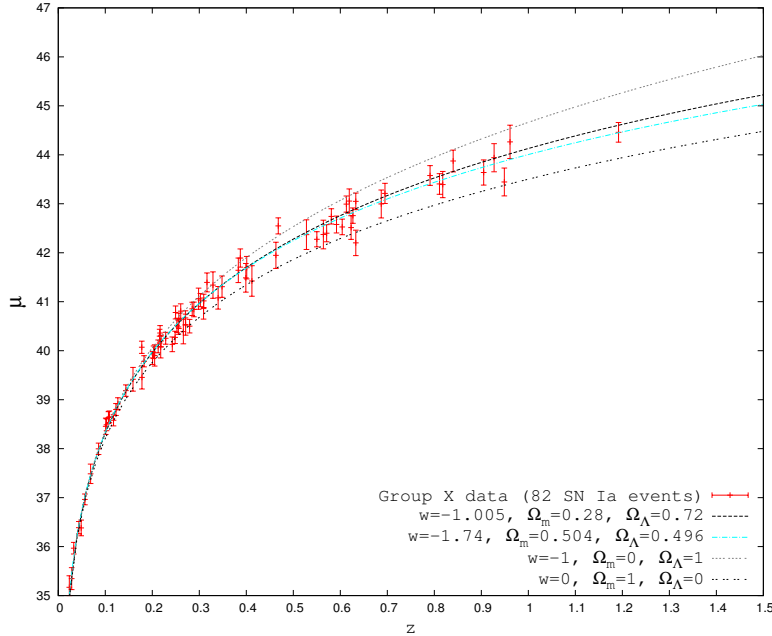

Figure 26: Distance moduli μ of Group X (82 SNe Ia) as a function of redshift and expected μ for four cosmological models.

This statistically important difference between Group X and the rest of the SNe Ia may be due to an anisotropy of the Hubble expansion in this area of the sky or due to some systematic observational error. In order to further investigate these possibilities, we

search the SNe Ia individual surveys that constitute the SNe Ia of Group X. We referred to the site;

$$http://astro.berkeley.edu/bait/public\_html$$

and we find that, from the 82 SNe Ia of Group X, there are:

- 36 SNe Ia from the Sloan Digital Sky Survey II (SDSS-II, 43.8% of the data) with redshift range $z \in [0.043, 0.387]$

- 19 SNe Ia from the Supernovae Legacy Survey (SNLS, 23.2% of the data) with redshift range $z \in [0.285, 0.961]$

- 18 SNe Ia from the Equation of State: SupErNovae trace Cosmic Expansion survey (ESSENCE, 22% of the data) with redshift range $z \in [0.205, 0.687]$

- 9 SNe Ia from several other surveys (2 from LOSS, 2 from HST, 1 from ESCC and 4 from individuals, 11% of the data) with redshift range $z \in [0.024, 1.192]$

A large amount of the Group's data was observed by the SDSS-II, so this survey has a dominant role to any results extracted from Group X. In addition, as we mentioned before, the SDSS-II contains SNe Ia with $z \leq 0.4$. ESSENCE and SNLS also play a key role to the results since each survey provide about 1/4 of the 82 SNe Ia and both have, especially SNLS, quite large redshifts.

To see how much the different sky surveys affect the final χ^2 minimization results, we perform the Jackknife Resampling method. Accordingly, we analyse the data of Group X excluding a certain subsample each time. To this end, we calculate the best-fit models and the 1σ contour plots for Group X, firstly without the SDSS-II data, secondly without the SNLS data and finally without the ESSENCE data. The results are:

- Group X without SDSS-II data (46 SNe Ia):

  $$w = -0.7875^{+0.1175}_{-0.1225} \quad , \quad \Omega_m = 0.256^{+0.076}_{-0.07} \qquad \text{with}$$

  $$\chi^2_{min}/d.o.f. = 47.637/ = 1.083$$

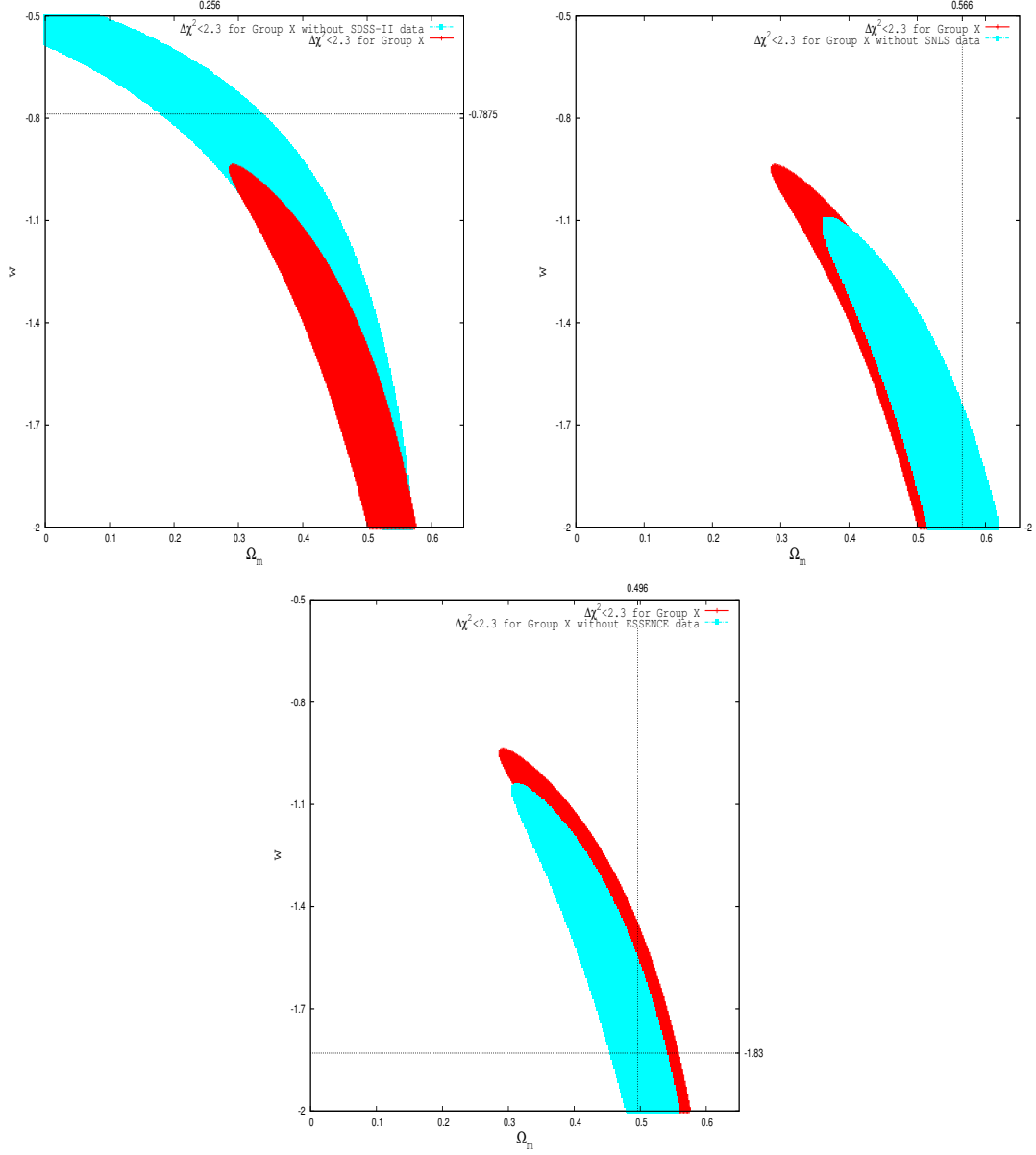**Figure 27:** 1σ contour plots for Group X (red contour) and for *Upper left panel:* Group X without the SDSS-II data (blue contour), *Upper right panel:* Group X without the SNLS data (blue contour), *Bottom center panel:* Group X (red contour) and for Group X without the ESSENCE data (blue contour).

- Group X without SNLS data (63 SNe Ia):

$$w = -2^{+0.345} \qquad , \quad \Omega_m = 0.566^{+0.052}_{-0.048} \qquad \text{with}$$

$$\chi^2_{min}/d.o.f. = 66.029/61 = 1.0824$$

- Group X without ESSENCE data (64 SNe Ia):

$$w = -1.83^{+0.2675}_{-0.17} \qquad , \qquad \Omega_m = 0.496^{+0.042}_{-0.038} \qquad \text{with}$$

$$\chi^2_{min}/d.o.f. = 76.767/62 = 1.238$$

The upper left panel of Figure 27 shows that excluding the SDSS-II data from the Group X, we obtain a dramatic shift of the 1σ contour with respect to that of Group X unlike the upper right and the bottom center panel, in which we have sequentially eliminated the SNLS and the ESSENCE data respectively. Without the SDSS-II data, the "banana-shaped" 1σ contour shifts to a more consistent position with respect to that of the whole SNe Ia. Moreover, excluding the SNLS or ESSENCE data, the SDSS-II subset becomes more dominant in Group X, causing the 1σ contour to shift into even more negative values of w and larger values of Ω_m. The conclusion that can be drawn from Figure 27 and from the above χ^2_{min} values is that this unusual behaviour of this sky region, is determined by the SNe Ia of the SDSS-II survey. In other words, responsible for this difference in the w-Ω_m solution behaviour between the sky region of Group X and the rest of the sky are the SDSS-II data in this region and not an actual anisotropy in the expansion. If there was an anisotropy in Hubble flow for this sky region, it should probably be seen also at all distant SNe Ia as well.

To see if there is a general systematic error in the SDSS-II survey, we compare the solution results of many other SDSS-II SNe Ia from the sky region where the SDSS-II focused from 2005 to 2007 (excluding Group X SNe Ia) as we mentioned in Section 3, with those of Group X. We remind the reader that this region is this characteristic "smile" in the southern galactic hemisphere or, in equatorial coordinates, $\alpha \in [20^h, 4^h]$ and $\delta \in [-1.25^o, 1.25^o]$. We set an upper limit in redshift, $0.02 < z \leq 0.4$ since this is the maximum redshift of SDSS-II data. Under these circumstances, 115 SNe Ia are left that we can use within these coordinates and redshift limits. Obviously, SNe Ia from other surveys can be included in these subsample but the vast majority of data comes from the SDSS-II, allowing us to extract conclusions regarding a possible systematic behaviour of the SDSS-II.
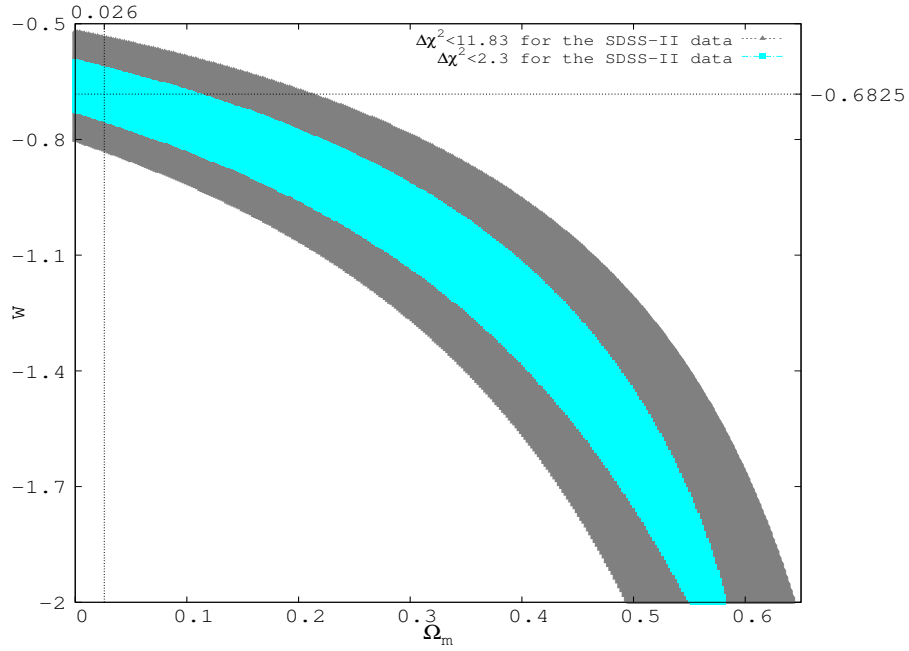
Figure 28: Solution space for w and Ω_m as it occurs from the analysis of the SDSS-II region without the data from Group X (115 SNe Ia). The blue contour corresponds to the 1σ confidence level (68.3%) and the grey to the 3σ confidence level (99.73%). The limits of the 1σ confidence level as well as the best-fit values are shown with the dashed lines.

The results are seen in Figure 28 where the best-fit parameter values are $w = -0.6825 \pm 0.0625$ and $\Omega_m = 0.026^{+0.078}_{-0.026}$ with $\chi^2_{min}/d.o.f. = 97.734/113 = 0.865$. Thus, all the other SDSS-II data provide a normal solution space behaviour compared with the SDSS-II from Group X. This probably means that the different behaviour of the Group X SNe Ia is not a result of some SDSS-II systematic error nor of an anisotropy in the Hubble expansion. We suggest as a possible solution of this unusual behaviour a large bulk flow attending the redshifts of the SNe Ia of Group X with $z \in [0.043, 0.387]$. We are currently investigating this possibility in detail

8 Conclusions

Several conclusions can be drawn based on the results of this thesis. First of all, high-z SNe Ia are necessary in order to distinguish the QDE cosmological models. Observationally, there are sky regions with far more SNe Ia than others, mainly in the southern galactic hemisphere. The best-fit cosmological parameters values with their 1σ uncertainties for the *Union2.1* sample, if we use the QDE cosmology model, are $\Omega_m = 0.28^{+0.02}_{-0.018}$, $w = -1.005 \pm 0.045$ and $q_0 = -0.501 \pm 0.086$, which is consistent with the other published results and the "concordance" cosmological model (Suzuki et al. 2012). We have searched for possible anisotropies of the Hubble expansion, by dividing the sample into different solid angles. We found no significant anisotropy in the Hubble expansion between the two galactic hemispheres. However, we identified a particular sky region, with galactic coordinates $35^o < l < 83^o$ & $-79^o < b < -37^o$, which provides a statistically significant different $w - \Omega_m$ solution with respect to the rest of the sample or any other subsample that we have analysed. Although this could have been attributed to an anisotropy in the Hubble flow, we found that this explanation is not supported by our analysis but rather this result could well be due to a large bulk flow of galaxies at this region within $z \sim 0.15 - 0.3$.

Appendices

A χ^2 minimization, our data analysis method

The most common statistical method to see how well a theoretical model describes observed data, is probably the χ^2 (chi-squared) minimization procedure. Below we describe the basics of this method which will be used throughout this thesis.

Suppose that we make a measurement (x_i, y_i) of a quantity y for a given x_i. The expected value for y_i according to the theory would be $f(x_i)$ and the total error of the experimental measurement (due to uncertainties of the measurement, etc.) would be σ. The probability to make this measurement is [1]

$$P(x_i) = \frac{1}{\sigma_i \sqrt{2\pi}} \exp\left[-\frac{1}{2} \left(\frac{y_i - f(x_i)}{\sigma_i} \right)^2 \right] \tag{A.1}$$

Now suppose that we make N measurements of this quantity that are independence of each other. The total probability of obtaining this entire set of these N data points is equal to the product of the probability of each data point (C. Laub, T. Kuhl), so

$$P_{tot} = \prod_{i=1}^{N} P(x_i) = \left[\prod_{i=1}^{N} \frac{1}{\sigma_i \sqrt{2\pi}} \right] \exp\left[-\frac{1}{2} \sum_{i=1}^{N} \left(\frac{y_i - f(x_i)}{\sigma_i} \right)^2 \right] \tag{A.2}$$

If we want to find the maximum probability we have to minimize the sum in the exponential term of P_{tot}, so, we define this quantity as

$$\chi^2 = \sum_{i=1}^{N} \left(\frac{y_i - f(x_i)}{\sigma_i} \right)^2 \tag{A.3}$$

and for χ^2_{min} we have the maximum probability. Thus, if the theoretical function $f(x_i, \mathbf{p})$, depends on a set of parameters, which correspond to the elements of the vector $\mathbf{p}$, we can test for which values of these parameters we get the maximum probability.

---

[1]Probabilities are normalized to their maximum values (Plionis et al. 2011)

In our case, y_i is the observed distance modulus of the each SN Ia, $\mu_{obs}(z_i)$, which comes with its redshift z_i. Furthermore, $f(x_i)$ is the theoretical expected distance modulus $\mu_{th}(z_i, \mathbf{p})$ for the same redshift z_i, with $\mathbf{p} \equiv (w, \Omega_m)$, for example. So, we have

$$\chi^2 = \sum_{i=1}^{N} \left(\frac{\mu_{obs}(z_i) - \mu_{th}(z_i, \mathbf{p})}{\sigma_i} \right)^2 \tag{A.4}$$

with σ_i being the error in the distance modulus μ_i of each SN Ia. As we said before, we have χ^2_{min} for the best-fitting parameters $\mathbf{p_0}$. When the parameters differ from these values, $\mathbf{p} \neq \mathbf{p_0}$, then χ^2 increases, so $\Delta\chi^2 = \chi^2 - \chi^2_{min} > 0$. Limits of $\Delta\chi^2$ that depend on the number of the fitted parameters N_f, define confidence regions that contain a certain fraction of the probability distribution of $\mathbf{p}$'s [1]. Almost every possibility region corresponds to a certain standard deviation σ. All these are shown in Table 5.

Table 5: $\Delta\chi^2$ limits for N_f fitted parameters and different confidence regions

σ	P	$N_f = 1$	$N_f = 2$	$N_f = 3$
1σ	68.3%	1	2.3	3.53
	90%	2.71	4.61	6.25
2σ	95.4%	4	6.17	8.02
3σ	99.73%	9	11.83	14.2

In order to see how good our fit is, we have to divide the minimum χ^2_{min} by the degrees of freedom, $d.o.f.$ and get the reduced chi-square, $\chi^2_{min}/d.o.f.$ If we have N data points and N_f fitted parameters, then $d.o.f. = N - N_f$. For a satisfactory fit we want $\chi^2_{min}/d.o.f. \approx 1$. In other words, our model describes the observational data very well, inside our uncertainties limits. If $\chi^2_{min}/d.o.f. \gg 1$ it means that our model is not an appropriate fitting function or that we have not taken into account some form of unknown systematic error. Finally, we may have underestimated our observational uncertainties (Bremer, 2009). On the other hand, if $\chi^2_{min}/d.o.f. \ll 1$, probably we have overestimated the

---

[1] For more information see "Numerical Recipes 3rd Edition: The Art of Scientific Computing", William H. Press

statistical uncertainties and systematics. As a result, the 1σ possibility will cover a very wide range of the fitted parameters, wide range of parameters, a non-desired effect.

B   Joint likelihood analysis

In joint likelihood analysis, we take n fully independent data samples. For every combination of (w, Ω_m) (we have a total of 195,000 combinations), we obtain a joint χ^2 which is given by

$$\chi^2 = \chi_1^2 + \chi_2^2 + \cdots + \chi_n^2 \tag{B.1}$$

while the degrees of freedom become

$$d.o.f. = d.o.f._{\cdot 1} + d.o.f._{\cdot 2} + \cdots + d.o.f._{\cdot n} \tag{B.2}$$

where $(\chi_1^2 \ldots \chi_n^2)$ are the values of χ^2 for every one of the n independent data samples while $(d.o.f._{\cdot 1} \ldots d.o.f._{\cdot n})$ are the degrees of freedom of the χ^2 analysis for every sample.

We then find the minimum, χ_{min}^2 and the deviation of all the others from it, $\Delta\chi^2 = \chi^2 - \chi_{min}^2$. Then, we plot the 1σ and 3σ contours ($\Delta\chi^2 \leq 2.3$ and $\Delta\chi^2 \leq 11.83$ respectively) as they occur from the joint analysis.

9 References

Aguirre, A. N. 1999a, ApJ, 512, L19

Aguirre, A., & Haiman, Z. 2000, ApJ, 532, 28

Amanullah, R., et al. 2010, ApJ, 716, 712

Basset, B.A. & Hlozek, R. 2009, arxiv.org/abs/0910.5224

Betoule M. et al., 2014, ArXiv e-prints

Bianchi, S., Ferrara, A., 2006, MNRAS, 358, 379 ApJ, 596, L135

Corasaniti, P.S., 2006, MNRAS 372,191

Davies, J. I., Alton, P. B., Bianchi, S., Trewhella, M., 1998, MNRAS, 300, 1006

Davis, Mörtsell, Sollerman and ESSENCE, 2007, astro-ph/0701510

Guy, J., et al. 2007, A&A, 466, 11

Hamuy, M., Phillips, M. M., Suntzeff, N. B., Schommer, R. A., Maza, J., & Aviles, R. 1996, AJ, 112, 2391

Hicken, M., et al. 2009c, ApJ, 700, 1097

Kim, A.G., et al. 1997, ApJ, 476, L63

Kowalski, M., et al. 2008, ApJ, 686, 749

Laub, C. & Kuhl, T. *A Critical Look at the Fitting of Reflectivity Models using the Reduced Chi-Square Statistic.* Retrieved from http://neutrons.ornl.gov

Ménard, B., Kilbinger, M., & Scranton, R. 2010, MNRAS, 406, 1815

Perlmutter, S., et al. 1998, Nature, 391, 51

Perlmutter, S., et al. 1999, ApJ, 517, 565

Planck Collaboration 2014 A&A 571, A16

Plionis M., Terlevich R., Basilakos S., Bresolin F., Terlevich E., Melnick J., Chavez R., 2011, MNRAS, 416, 2981

Riess, A. G., et al. 1998, AJ, 116, 1009

Riess, A. G., et al. 1999, AJ, 117, 707

Riess, A. G., et al. 2004, ApJ, 607, 665

Riess, A. G., et al. 2007, ApJ, 659, 98

Ryden, Barbara. *Introduction to Cosmology.* Ohio State Uni., 2003

Varvoglis, H & Seiradakis, J.H.,: *Introduction to modern Astronomy*, Thessaloniki: Gargatanis
, 1994

Shustov, B. M., Vibe, D. Z., 1995, Astronomy Reports, 39, 579

Sullivan, M., et al. 2003, MNRAS, 340, 1057

Sullivan, M., et al. 2006, ApJ, 648, 868

Sullivan, M., et al. 2010, MNRAS, 406, 782

Suzuki N. et al., 2012, ApJ, 746, 85

Wu, P., Zhengxiang, L. & Hongwei, Y., 2015, arXiv:1501.01818

Yoon, S.C. & Langer, N., 2004, Astron.Astrophys.435:967-985,2005